Z. Phys. B – Condensed Matter 69, 347–377 (1987)

Condensed
Zeitschrift für Physik B Matter

Phase Diagram and Phase Transitions of Krypton on Graphite in the Extended Monolayer Regime

E.D. Specht[1], A. Mak, C. Peters, M. Sutton[2], and R.J. Birgeneau
Department of Physics, Massachusetts Institute of Technology, Cambridge, Massachusetts, USA

K.L. D'Amico[3] and D.E. Moncton[3]
Brookhaven National Laboratory, Upton, New York, USA

S.E. Nagler[4] and P.M. Horn
IBM T.J. Watson Research Center, Yorktown Heights, New York, USA

Received April 27, 1987

We report high resolution x-ray diffraction studies of the structures and phase transitions of monolayer krypton, adsorbed on both powder and single crystal graphite substrates. A comprehensive series of powder diffraction profiles is used to construct the two dimensional phase diagram. The melting of the $\sqrt{3} \times \sqrt{3}$ commensurate solid is shown to be strongly first order throughout the region where tricritical behavior was previously thought to occur; fluid solid coexistence extends up to the termination of the commensurate phase at 130 K. A disordered weakly incommensurate phase is shown to be a reentrant fluid, a system which may be described as a disordered network of domain walls and which evolves continuously into a more conventional 2D fluid. This evolution is marked by the disappearance of satellite peaks which are caused by the modulation of the overlayer by the substrate. The freezing of the reentrant fluid into the commensurate phase is shown to be consistent with a chiral Potts transition, its freezing into the incommensurate solid consistent with a dislocation binding transition.

Single crystal experiments reveal the orientation of the weakly incommensurate phase. The reentrant fluid is found to have no visible orientational fluctuations, manifesting isotropic diffraction peaks. This is attributed to the strong epitaxy of domain walls. The incommensurate solid is shown to undergo an aligned-rotated transition which is well described by zero-temperature calculations.

I. Introduction

Two dimensional (2D) behavior has been observed in a wide variety of systems; reference [1] discusses surfaces, interfaces, thin films, intercalation compounds, liquid crystal systems, Wigner crystals, magnetic systems, membranes, and micelles. These systems are

[1] Present address: Metals and Ceramics Division, Oak Ridge National Laboratory, Oak Ridge, TN 37831, USA
[2] Present address: Department of Physics, McGill University, Montreal PQ H3A 2T8, Canada
[3] Present address: Exxon Research and Engineering Co., Annandale, NJ 08801, USA
[4] Present address: Dept. of Physics, University of Florida, Gainesville, FL 32611, USA

anisotropic, with long range order developing in two dimensions while there is only finite order in the third. For many of these systems the shift from 3D to 2D ordering produces drastic changes in the phases themselves and in their critical behavior. Critical exponents typically change with dimension, and below a lower marginal dimensionality thermal fluctuations destroy long range order entirely.

Rare gases adsorbed on graphite basal planes have proved a rewarding experimental system for the study of 2D phase transitions. Monolayer films are readily prepared, and phase changes may be induced by varying temperature and the areal density of adsorbate. The simple, isotropic interaction between the adsorbed rare gas atoms facilitates the application of a wide variety of theoretical calculations. For the same reasons, these are simple systems in which to study the effect of the symmetry of the substrate on 2D systems. One may also study ordering in monolayer, bilayer, and progressively thicker films. This will elucidate the approach to 3D behavior caused by coupling between layers. As a prototypical problem, monolayers of rare gases on graphite typically melt in a continuous phase transition peculiar to 2D systems, while 3D rare gas solids always melt in first order transitions: we do not know the behavior of films of intermediate thickness.

To-date, most progress has been made studying the effect of the substrate periodicity on the monolayer phase. While the rare gas atoms are tightly bound to the graphite surface, the adsorbate-substrate potential is only weakly corrugated in the plane of the surface, with the periodicity of the 3D graphite lattice. The monolayer may be treated as a 2D system under the influence of a field with the long range order characteristic of the 3D substrate.

The strength of the perturbation of 2D order by the graphite substrate varies with different rare gas adsorbates; the interaction potentials are not so different, but the mismatch between the substrate and adsorbate periodicity varies greatly. Only in the case of krypton does the monolayer form a solid, stable to high temperatures, with lattice constant commensurate with the substrate. By varying temperature and Kr pressure, the lattice mismatch may be varied, spanning the range from strong coupling to the substrate when the mismatch is small to weak coupling for large mismatch. Krypton on graphite (Kr/Gr) therefore provides a complex phase diagram which, combined with the simple interactions, provides an ideal testbed for theories of interactions on competing length scales.

As first shown by a detailed series of adsorption isotherms carried out by Thomy and Duval [2, 3, 4], monolayer Kr/Gr exhibits solid, liquid and gas phases with a critical and a triple point, as in a typical 3D phase diagram. Their phase diagram differs in two major ways from the 3D phase diagram of Kr, however. Firstly, the liquid-solid coexistence region narrows at higher temperatures and pressures, disappearing at about 100 K in a tricritical point. Below this tricritical point the phase transition is first order: density is discontinuous as a function of temperature and pressure. At the first order transition temperatures, islands of the solid phase grow in coexistence with a more dilute gas. Above the tricritical point, density varies continuously while its derivative is discontinuous: the transition is second order.

Secondly, a second order phase transition can be seen within the solid phase. At lower densities the lattice constant of the solid is commensurate with that of the substrate, with the structure shown in Fig. 1a. At higher densities the overlayer is compressed relative to the substrate, that is, incommensurate.

Both the tricritical region and the commensurate–incommensurate transition have been the subject of much study since Thomy and Duval's initial reports, the principal goal being to understand the details of these phase transitions. At the same time, understanding of the phase diagram developed. In 1980 a heat capacity study by Butler, Litzinger, and Stewart [5] showed that the commensurate solid phase terminates at 130 K (Fig. 2). The commensurate solid (C), incommensurate solid (IC), and fluid (F) phases

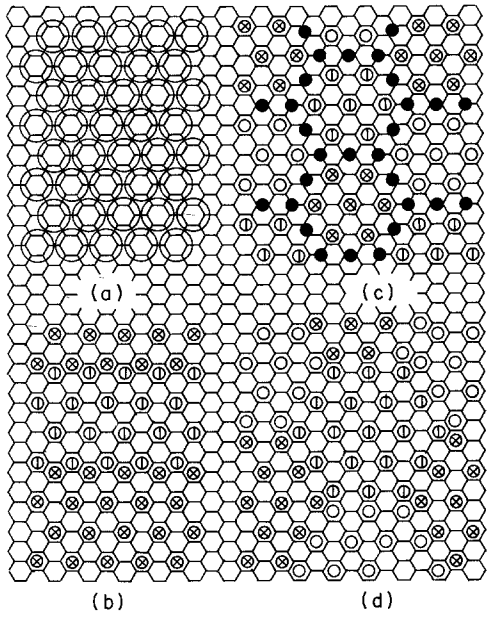

Fig. 1a–d. Domain structures in the limit of a strong Kr-Gr potential. Atoms on the three sublattices are indicated by different symbols, solid circles denoting atoms between domains. **a** Commensurate phase, with atoms drawn to scale. **b** Uniaxial array of superheavy domain walls. **c** Hexagonal array of superheavy domain walls; location of walls relative to the substrate is different to **b**. **d** Hexagonal array of heavy domain walls

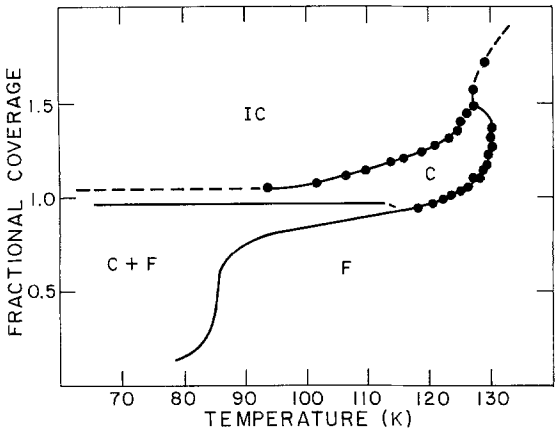

Fig. 2. Kr/Gr phase diagram, after [5]. Solid circles are heat capacity anomalies, submonolayer phase boundaries are found from adsorption isotherms. Dashed lines indicate extrapolated features. F, C, and IC denote fluid, commensurate, and incommensurate solid phases

were taken as meeting in a multicritical point. With increasing temperature the C-F and C-IC boundaries increase in coverage to ~1.5. Their unit of coverage corresponds to the quantity adsorbed in a compressed monolayer at 77 K, or 1.1 commensurate monolayers. Apparently the strongly first-order phase transitions between monolayers, bilayers, and so forth do not extend to high temperature. The phase transitions occurring in the monolayer at low temperatures now move to higher coverages: Butler et al. call this the extended monolayer regime.

Their claim to have completed the extended monolayer phase diagram proved short-lived, however. Several months later a LEED study [6] found that the incommensurate solid was aligned with the Gr lattice only at densities very close to the commensurate phase. At higher densities it appeared to rotate away by half a degree. Meanwhile, synchrotron x-ray diffraction studies of the C-IC transition [7, 8] found the IC phase to be disordered near the C phase. Thus the IC region of Fig. 2 comprises three phases, with a rotated-aligned and an ordered-disordered transition within it.

These two discoveries motivated this paper, which reports a series of high resolution x-ray diffraction studies of Kr/Gr. We will incorporate these new phases into a phase diagram which is still not complete, but consistent with current data. We examine the phase transitions to the rotated phase and the disordered weakly incommensurate phase in detail; we also report surprising new results concerning the much-studied tricritical behavior, implying a tricritical point occurring at a much higher temperature than previously reported. These discoveries were made possible by using synchrotron x-ray sources bright enough to study even a single layer of atoms with resolution otherwise possible only for polycrystalline samples. In Sec. II we summarize the diffraction patterns expected from 2D systems and describe the x-ray diffraction apparatus used. Section III describes an experiment using a polycrystalline graphite substrate, which gives much structural information but cannot describe the orientation of the Kr overlayer. Thus we proceeded to experiments using single crystal substrates, described in Sect. IV. Two brief reports have been made of this work [9, 10].

II. X-Ray Scattering

IIA. Diffraction from 2D Structures

Before describing our actual x-ray diffraction apparatus, we will summarize the scattering we expect from a variety of 2D structures. A 2D crystal with delta function Bragg peaks can form only in a commensurate system, where the overlayer acquires the long range order of the substrate surface. For an incommensurate system, where the lattice is fully invariant under translation (but not rotation), atomic displacements diverge logarithmically with system size due to long wavelength phonons, instead of approaching a constant value as for a commensurate overlayer. Delta function singularities in the structure factor are replaced by power-law singularities, reflecting algebraic order [11–14]:

$$S(\mathbf{Q}) \sim \sum_{\mathbf{G}} A_{\mathbf{G}} |\mathbf{Q}-\mathbf{G}|^{\eta_{\mathbf{G}}(T)-2}, \tag{1}$$

where

$$\eta_{\mathbf{G}}(T) = kT|\mathbf{G}|^2 \frac{3\mu+\lambda}{4\pi\mu(2\mu+\lambda)}; \tag{2}$$

λ and μ are the Lamé coefficients of the overlayer. Despite the lack of long range positional order, the incommensurate solid retains a rigid lattice with nonzero shear modulus, and long-range orientational order, that is, well-defined crystalline axes [11, 12, 13].

The melting of such an incommensurate solid can proceed in two stages, a possible mechanism being the successive unbinding of dislocations and disclinations [14]. The intermediate state has algebraic orientational order but short range positional order: for systems with 6-fold rotational symmetry it is called *hexatic*.

As we shall discuss below, the substrate will convert the orientational order from algebraic to truly long range. To explore the hexatic phase we must measure both kinds of ordering. Positional correlations are measured directly by the structure factor $S(\mathbf{q})$: a

correlation length ξ gives a structure factor with longitudinal width $\kappa \sim 1/\xi$. The degree of orientational order is not simply the reciprocal of the transverse width however; this width reflects the amplitude of orientational fluctuations.

Following Nelson [15], we may treat orientational fluctuations in a hexatic phase using a harmonic approximation. Long wavelength fluctuations will dominate, with the mean square amplitude diverging logarithmically with system size. We may consider regions Λ with length scales larger than the positional correlation length ξ but smaller than the system size. Orientational fluctuations within regions smaller than ξ will not be important. For perfect orientational order, in the harmonic approximation, the structure factor is given simply by

$$S_\Lambda(\mathbf{Q}) = \langle |\rho_\Lambda(\mathbf{Q})/^2 \rangle = \frac{C}{\kappa^2 + (\mathbf{Q}-\mathbf{Q}_0)^2}. \tag{3}$$

where

$$\rho_\Lambda(\mathbf{Q}) = \frac{1}{N}\sum_\Lambda e^{i\mathbf{Q}\cdot\mathbf{r}_i}. \tag{4}$$

In the hexatic phase, (3) should be averaged over orientational fluctuations.

At reduced temperature $t = (T - T_c)/T_c$, in the hexatic phase just above the solid-hexatic transition, renormalization-group calculations for the dislocation unbinding transition give [14]

$$C \sim C_0 t^{\eta_{\mathbf{G}}(T_c)}, \quad \kappa \sim \kappa_0 e^{-B/t^\nu}. \tag{5}$$

For the lowest reciprocal lattice vector G_0, $\eta_{\mathbf{G}_0}(T_c)$ lies between $\frac{1}{4}$ and $\frac{1}{3}$, depending on the value of Poisson's ratio for the solid. Similarly, ν may lie between 0.37 and 0.40.

For small orientational fluctuations, the free energy of a hexatic will be

$$F = \int d^2r (f_\Lambda + \tfrac{1}{2}K_A|\nabla\theta|^2 + \tfrac{1}{2}h_6\theta^2), \tag{6}$$

where f_Λ is the free energy density due to fluctuations within region Λ, θ is the orientation of domain Λ relative to the substrate, K_A is a Frank constant of magnitude $kT\xi^2$, and h_6 is the orienting field due to the substrate [14]. Integrating over orientational fluctuations on length scales between the positional correlation length ξ and the system size L, the domain's orientation will take a Gaussian distribution with width

$$\langle \delta\theta^2 \rangle = \frac{kT}{4\pi K_A} \ln \frac{K_A q_c^2 + h_6}{K_A q_L^2 + h_6}, \tag{7}$$

where $q_c = \left(\frac{2}{\pi\sqrt{3}}\right)^{1/2} \frac{2\pi}{\xi}$ and $q_L = \frac{2\pi}{L}$ [16]. This form gives the Lorentzian (3) convoluted with a Gaussian for the transverse structure factor. In the limit of weak substrate coupling, fluctuations diverge logarithmically with the size of the system, L, giving for a large system an isotropic ring of scattering with a structure factor which is approximately the square root of a Lorentzian. Since the divergence is only logarithmic with system size, it should still be possible to observe a well-oriented sample of macroscopic size.

At still higher temperatures the overlayer will lose orientational as well as positional order. Well above the hexatic-isotropic transition, the structure factor may take on the form

$$S(\mathbf{Q}) \simeq \frac{kT}{\kappa^2 + (|\mathbf{Q}| - Q_0)^2}. \tag{8}$$

Rather than Lorentzian spots, the structure factor may exhibit rings about the origin with a Lorentzian cross-section. For the solid, the hexatic, and the fluid, the longitudinal width of the structure factor peak gives a measure of the positional correlation length. No such information can be extracted from the transverse width of the peak; if the orientational correlation length diverges in a fluid with constant positional correlation length, the structure factor will not change significantly, remaining a complete ring of constant width for all temperatures above the hexatic-fluid transition.

Since the overlayer lies on an ordered substrate, it will have long range orientational order for all cases although the orienting field h_6 may be weak. The hexatic has a divergent susceptibility to the orienting field; however, in the fluid phase the susceptibility is finite, so a small h_6 will produce only a weak six-fold modulation in the rings of scattering. For a larger h_6 or a better correlated fluid, orientational fluctuations will be suppressed: taking the limits $K_A \to 0$, $L \to \infty$ in (7),

$$\langle \delta\theta^2 \rangle = \frac{2kT}{\sqrt{3h_6\xi^2}}. \tag{9}$$

As for a paramagnet-ferromagnet transition in an applied magnetic field, the substrate field will smear out a hexatic-isotropic transition; the solid-hexatic transition will remain sharp.

IIB. X-Ray Sources

We have overcome the small cross-section of a Kr monolayer in two ways. By using exfoliated substrates we greatly increase surface area [17]. Since orientational information is thereby lost, experiments using single crystal substrates must be carried out as well; here the scattering cross-section is increased by the large coherence length of our overlayer. We require a well-collimated, monochromatic x-ray source to take

advantage of the sample coherence, and a well focussed beam to illuminate a small sample. In any case, a bright beam is needed, although the simple expedient of more photons increases the background scattering from the substrate as well as the signal.

The experiments described herein were carried out at two facilities providing such an x-ray source, first at beamline VII-2 at the Stanford Synchrotron Radiation Laboratory (SSRL), a wiggler end station which has been described previously [18], then at the newly completed IBM-MIT beamlines at the National Synchrotron Light Source (NSLS).

The IBM-MIT beamlines are built on one bending magnet at NSLS. At 9 keV the x-ray flux produced by a typical stored electron beam of 100 mA at 2.53 GeV is $1.4 \times 10^{13} \frac{\text{photons}}{\text{s}\,0.1\%\,\text{BP}}$ distributed uniformly over the 5 mrad horizontal acceptance of each beamline but with only 0.11 mrad HWHM vertical divergence; due to a higher electron beam energy and the use of an 8-pole wiggler rather than a bending magnet, the corresponding figure at SSRL was 2.0×10^{14} [19].

In their basic design, the two IBM-MIT beamlines are similar to that used at SSRL: an ellipsoidal mirror in a 1:1 focussing geometry is followed by a double crystal monochromator. Each beamline consists of evacuated pipe up to a radiation protection hutch. Beryllium windows seal either end, one between our beamlines and the storage ring vacuum, the others in the radiation protection hutches. Attenuation by these windows seriously diminishes the x-ray flux below ~4 keV. Evacuated flightpaths are added before and after the cryostat holding the sample to minimize air scattering. All components exposed to white beam, that is up to the first monochromator crystal, are water cooled.

The x-ray beam is focussed in both the horizontal and vertical directions by a single mirror, a single crystal block of silicon $60 \times 10 \times 4$ cm^3. It is ground to a cylindrical figure with an 8 cm radius of curvature, then coated with platinum over a rhodium base. Total external reflection occurs below a critical energy of 12.1 keV for a glancing angle of 0.4°, with reflectivity falling off sharply at higher energies.

The low reflectivity above the critical energy typically provides an important advantage. The synchrotron is a broad-band source, and monochromator crystals will reflect higher harmonics: a Si(111) crystal set for 9 keV will reflect 27 keV x-rays from the (333) planes in the same direction. Thus in the absence of the mirror we see a spurious 27 keV Gr(110) peak obscuring the weaker 9 keV Kr(100). The mirror removes these higher harmonics: at three times the critical energy the Fresnel reflectivity is only 8×10^{-4}.

The focus of the mirror is critical, since NSLS provides a compact source, 0.38 mm horizontal $\times$ 0.12 mm vertical. As noted above the mirrors on our two beamlines, X20A and X20C, are each ground with a fixed sagittal radius of 8 cm; to obtain 1:1 focussing at focal distances of 6.4 and 5.4 m respectively, they are each bent in situ by four spring loaded rods with meridional radii of 2.0 and 1.5 km and tilted to glancing angles of 0.35° and 0.44°. This experiment used beamline X20A.

A horizontal 4 milliradian beam is focussed into a final spot size of 1.1 mm horizontal $\times$ 0.71 mm vertical, a factor of 17 larger than that for an ideal mirror. The effect of the larger spot size on this experiment was to dictate the use of a larger, less perfect crystal. The SSRL source is 4 mm $\times$ 1 mm so focus is not as critical; we can take full advantage of the greater intensity of the SSRL wiggler source only for a sample several mm in size.

We use a double crystal monochromator, with scattering in the vertical plane. Each crystal has two rotational degrees of freedom, one to tilt the normal to the crystal planes into the scattering plane, the other to rotate the crystal in the scattering plane to select the energy. The rotation and tilt are effected by high-precision goniometers inside the beamline vacuum. The downstream crystal has a fine adjustment to its rotation controlled by a piezoelectric crystal to compensate for small thermal shifts of the upstream crystal. As the x-ray energy is changed, the downstream crystal is moved parallel to the beam so as to intercept it at the right height. Energy is calibrated within 1 eV by locating the Cu K absorption edge at 8.979 keV at NSLS, the 7.112 keV Fe K edge at SSRL.

The NSLS experiment used Si(111) monochromator crystals with 0.0018° Darwin width; at SSRL we used asymmetrically cut Ge(111) crystals, giving higher flux but poorer resolution. By using an oppositely aligned pair in a double crystal monochromator, each cut at 7° from the (111) face, the upstream crystal decreases angular divergence and increases beam size, while the downstream crystal restores the original beam parameters, the only net effect being an increased bandpass for the monochromator. Flat Ge(111) crystals have a 0.005° Darwin width, versus 0.013° when asymmetrically cut. Both experiments used flat Ge(111) analyzer crystals. Thus instrumental reciprocal space resolution was 3.6×10^{-4} Å^{-1} HWHM longitudinal, 7.0×10^{-5} Å^{-1} transverse at NSLS, the resolution was somewhat broader at SSRL.

Each beamline is equipped with 32 stepping motors controlling 4 horizontal and 4 vertical beam apertures, 2 fluorescent screens and 2 ion chambers which may be inserted into the beam, mirror position and orientation, the monochromator and the diffractometer. An

IBM PC-XT microcomputer running a Venix operating system controls a CAMAC crate housing 4 Data Signal Processing E500 stepping motor controllers, each of which generates pulse trains for 8 stepping motors. Pulses for each set of 8 motors are carried to an Advanced Control Systems MDU-8 Step-Pak, which provides the 6-phase driving voltages.

Experiments are mounted on a Huber 6-circle diffractometer, which rests on a table providing translation in the horizontal and vertical directions, transverse to the beam, with an accuracy of 0.01 inch. We have developed a program to control the diffractometer, as well as all other motors. This allow us to scan all spectrometer circles and to scan beam energy. Applying the algorithms of Busing and Levy [20], sample orientation may be determined by locating two Bragg peaks; then reciprocal space scans may be taken. Since the diffractometer has an extra degree of freedom, one of several constraints must be applied. One of the three circles determining sample orientation may be held fixed, or an azimuth angle describing rotation of the sample about the reciprocal lattice vector may be fixed.

A NaI scintillation detector was used to count scattered x-rays. A pulse height analyzer provided $\sim 30\%$ energy resolution. While count rates are reported in counts/second, counting time was in fact normalized to a beam monitor: a thin film of Kapton placed diagonally in the incident beam scatters into a similar detector. Counting time is inversely proportional to stored electron current, with a nominal second of 100,000 monitor counts corresponding to a real second at 140 mA. Typical stored electron beam current was 120 mA at both sources, decaying to 40 mA over 4 h.

III. Powder Experiments

Due to the high surface area of an exfoliated substrate, we were able to make an extensive survey of the high-temperature region of the extended monolayer regime in a two week run at SSRL. The dashed lines in Fig. 3 indicate paths through the phase diagram along which we have taken detailed series of scans. We find a phase diagram strikingly different from that found by Butler et al. [5]. Rather than a C-F and a C-IC transition, joining at a multicritical point, we find a single transition from commensurate to fluid phase; at constant pressure the fluid first freezes into a commensurate solid, then reenters the fluid phase before freezing again into an incommensurate solid. To understand this behavior we will first review previous results regarding the C-F and C-RF transitions, then describe their evolution as they join.

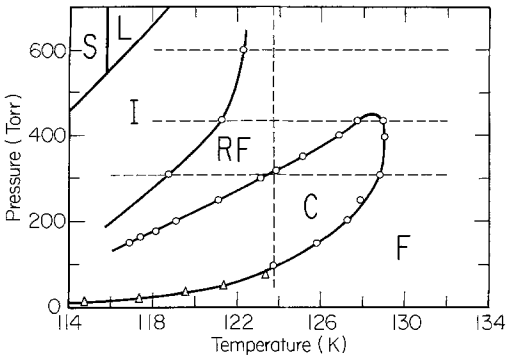

Fig. 3. Kr/Gr phase diagram: F—fluid, C—commensurate solid, RF—reentrant fluid, IC—incommensurate solid, S—3D solid, L—3D liquid. Triangles are from [22], circles this work. Scans were taken along dashed lines

IIIA. Review

As may be seen from Fig. 2, the C-F transition is strongly first order below 85 K, while at higher temperatures there is an extended region with a small discontinuity in coverage, less than 10%. Thus while early adsorption isotherms experiments located a tricritical point a temperature $T_3 \approx 95$ K [4, 21], progressively more refined measurements have traced the coexistence region up to 117 ± 2 K [22, 23]. It is difficult to tell, simply by measuring the width of the C-F coexistence region, whether it disappears or narrows beyond experimental resolution. Even when experimental variables such as temperature, pressure and coverage are precisely controlled, phase transitions remain rounded due to impurity and imperfection of the substrate. Using thermodynamic measurements such as adsorption isotherms and heat capacity, weakly first order and second order transitions are prohibitively difficult to distinguish. Suter et al. [23] found that the shape of the nominally vertical step in coverage at lower temperatures where the C-F transition is unambiguously first order may be described by a Gaussian distribution of transition chemical potentials with 1.5 K FWHM, for ZYX graphite. This corresponds to $\Delta P/P \approx 0.015$ or $\Delta T/T \approx 0.003$. At 119 K the step in the isotherm can no longer be fit to a first order jump convolved with this distribution (the transition width is roughly doubled), so Suter et al. [23] conclude that the transition is second order, with $T_3 = 117 \pm 2$ K. However, the nature of the fluid at the phase boundary is evolving rapidly in this region, increasing in density. This might have a large effect on the susceptibility of the transition to inhomogeneity. It should also be noted that in the system of nitrogen on graphite which has a phase diagram closely analogous to that of krypton, Miner et al. [24] have demonstrated

that the commensurate solid-fluid transition is first order up to the highest temperatures.

X-ray diffraction measurements of Bragg peak intensity illustrate the difficulty of distinguishing between a first order transition smeared by inhomogeneity and the power law behavior of a second order transition. Data have been reported which are consistent with critical behavior both at and above T_3. Bragg peak intensity will be zero in the fluid, increasing linearly across a coexistence region for a first order transition and growing as a power law $I \sim (T-T_c)^{2\beta'}$ through a second order phase transition for fixed coverage scans. Apparent power law behavior has been observed at 106 K with $\beta' = 0.09 \pm 0.03$ [25] and at 113 K with $\beta' = 0.065 \pm 0.015$ [26]. Although both sets of data are consistent with power law behavior, adsorption isotherms strongly suggest that the lower temperature transition is first order [22, 23].

As we shall see, x-ray scattering studies of the fluid and solid phases can give less ambiguous results. For a strongly first order transition, there is little evolution of the lineshape of either phase; while inhomogeneity will broaden the transition over a distribution of temperature or pressure, diffraction profiles near the transition will show a simple linear combination of the two phases. For a second order transition the correlation length in the disordered phase diverges as the transition is approached; diffraction profiles from an imperfect sample will reflect a distribution of peaks of various widths. There is a more qualitative difference between first and second order transitions, so results are less dependent on detailed modelling of the transition.

As may be seen from Fig. 1a, Kr atoms in the commensurate lattice occupy one third of the hexagonal Gr sites: they may occupy any one of three sublattices. The C-F transition falls in the three-state Potts universality class. Berker et al. have developed a renormalization group treatment of the three-state Potts lattice gas, applied to this transition [27]. A four-state variable is assigned to each group of three sites: three values correspond to the three sublattices, the fourth to either a vacancy (as for a bare surface) or random occupancy (as for a dense fluid). Renormalization calculations give a phase diagram with a tricritical point at 108 K. Calculated exponents for sublattice occupation are consistent with the x-ray measurements of Bragg peak intensity [25, 26], $\beta' = 0.100 \pm 0.004$ above and $\beta' = 0.083$ at the tricritical point.

The Potts lattice gas model does not explain the extended narrow coexistence region. Ostlund and Berker [28] have produced a phase diagram with a cusped coexistence region in better agreement with observed phase boundaries. They suggest that the true tricritical point is 78 K. An apparent coexistence region is observed due to sample inhomogeneity: while an adsorption isotherm at a second order transition is continuous, its slope diverges, and there will be a substantial jump in coverage over the range ΔT in which the transition is smeared. Again, by looking for a diverging correlation length in the fluid phase, we hope to resolve the ambiguity surrounding this elusive tricritical point.

While the C-F transition was immediately recognized as a melting transition, the C-RF transition was initially characterized as a transition from commensurate to incommensurate solid [29]. However, the first synchrotron x-ray study of this system by Moncton et al. [8] showed that at least above 80 K, a disordered phase intervened between the two solid phases. They also showed that as pressure is increased at constant temperature, the misfit follows a universal form:

$$m = \frac{a_0 - a}{a_0} = A[T \ln(P/P_c)]^{\beta}; \tag{10}$$

P_c is the pressure at the C-RF transition, a_0 and a the lattice constants of commensurate and incommensurate Kr; $A = 0.79\%$ and $\beta = 1/3$ describe the misfit over the entire temperature range [8, 29, 30]. This behavior continues smoothly through the RF-IC transition, saturating at 5% misfit when the 3D solid Kr lattice constant is reached.

The incommensurate solid has hexagonal symmetry like the commensurate solid and the (111) face of the 3D solid. However, the IC phase is modulated by the substrate, giving rise to satellite peaks in the diffraction pattern. The satellite peak intensity reflects the amplitude of this modulation. At large misfit the distortion is small and may be treated as a sinusoidal perturbation, while at small misfits the structure is better described as a honeycomb network of discommensurations separating commensurate domains. X-ray diffraction measurements by Stephens et al. [30] of satellite peak intensity are consistent with a domain wall width of 5.7 ± 1 Kr rows, independent of misfit [30].

In their high resolution x-ray diffraction measurements, Stephens et al. [30] show that the weakly incommensurate phase is disordered. At 94.0 K, the maximum peak half-width κ of 0.005 ± 0.001 Å^{-1} occurs at the smallest misfit observed, 1.2%. Thus while the continuous power-law behavior of the misfit suggests that the transition is second order, the correlation length shows, within experimental resolution, a discontinuous jump to its lowest value. The incommensurability, defined as $\varepsilon = q - q_0$ where q and q_0 are the Kr(100) reciprocal lattice vector (r.l.v.) in the incommensurate and commensurate phases respectively,

is of the same order as the inverse correlation length κ: this reflects disorder on the length scale of the domain wall separation. In contrast to its jump at the C-RF transition, κ decreases gradually through the RF-IC freezing transition.

A simple model of the C-IC transition at zero temperature was proposed by Frank and van der Merwe [31]. In this 1D model, the Kr adsorbate is represented by a 1D harmonic lattice, while the substrate provides a sinusoidal potential. The natural lattice constant of the overlayer, that is, that with no substrate effect, is taken to vary linearly with pressure, and the system is treated using a continuum approximation. The model then predicts a continuous C-IC transition as a function of pressure, with misfit $m \sim \left(\log \frac{1}{P-P_c}\right)^{-1}$. The Frank and van der Merwe model explains the abrupt but continuous commensurate-incommensurate transition, but the observed 1/3 power-law misfit [8, 29, 30] does not agree with the predicted logarithmic dependence.

One way to make the model more realistic is to include the two dimensionality of the system. Again using a continuum approximation, Shiba has numerically minimized the energy of a harmonic hexagonal 2D lattice distorted by a Gr substrate [32, 33]. The 2D Kr-Gr potential used by Shiba is

$$V(\mathbf{R}) = -V_0 \sum_{i=1}^{3} \cos(\mathbf{K}_i \cdot \mathbf{R}), \tag{11}$$

where the three $\mathbf{K}_i$ are the Gr(100), (010), and (001) r.l.v. Calculations of the rare gas-graphite interaction [34, 35] suggest that this form accurately describes the potential. More restricted energy minimization calculations for a discrete lattice with the same Kr-Gr and a realistic Kr-Kr interaction [36] are consistent with Shiba's results, confirming that the approximation of the Kr overlayer by a harmonic lattice is reasonable. The overlayer is described by two Lamé coefficients λ and μ, where $\lambda = \mu$ for a Cauchy solid. The model gives quantitative agreement with (10) with one free parameter, the domain wall width $l_0 = [2(\lambda + 2\mu)/(3V_0)]^{1/2} \approx 32$, corresponding to a width of 4.8 rows, agreeing with the Stephens et al. [30] value of 5.7 ± 1, calculated from satellite peak intensity. Agreement of the calculated misfit with a power law is accidental: the misfit varies logarithmically with pressure near the transition, crossing over to a linear dependence for large misfits. This suggests that the temperature independent behavior of the misfit observed in experiment may be due not to the universality of critical behavior, but to the low temperatures involved. On the other hand, the temperatures, however, are not small compared to the interaction energies involved.

As a further complication, several domain wall structures are possible. Because commensurate Kr may occupy any of three sublattices, two types of domain wall may form. For an overlayer denser than the commensurate phase, the walls may be heavy (Fig. 1d) or superheavy (Figs. 1b, c). Kr rows parallel to the wall move together by 1/3 of a row spacing at a heavy wall, 2/3 at a superheavy wall. A more qualitative difference is that the superheavy wall introduces only a strain in the hexagonal Kr lattice, while the heavy wall puts in a row of interstitial atoms. In the limit of a weak substrate potential the superheavy wall can relax continuously to an unperturbed lattice, so it will have lower energy. Since Shiba's calculation considers only lattice strains, not defects, it implicitly assumes superheavy walls. Energy minimization calculations comparing heavy and superheavy wall configurations confirm that superheavy walls are favored [36], as shown by the earlier diffraction experiments [8, 30].

Each type of wall can be arranged in a honeycomb network with hexagonal symmetry (Figs. 1c, d) or a uniaxial array of parallel walls (Fig. 1b). Shiba's calculation indicates that the domain walls will be uniaxial for small incommensurability, hexagonal for larger incommensurability. Renormalization group calculations [37] predict, however that the uniaxial phase is stable only below 50 K, which might explain why only the hexagonal phase has been observed experimentally.

A more phenomenological approach is to consider the statistical mechanics of domain walls rather than of Kr atoms. Bak et al. [38] use mean field theory to treat the zero-temperature case of a harmonic lattice of domain walls. The nature of the transition depends on the wall crossing energy Λ: Λ positive leads to a first order transition to a hexagonal incommensurate phase, Λ negative to a second order transition to a uniaxial phase, followed by a first order transition from uniaxial to hexagonal. The observed case, a continuous transition to a hexagonal phase, is ruled out.

At non-zero temperature, the long range interaction energy between domain walls may be ignored. In the case of hexagonal domain walls, for large wall separations, the dominant interaction term derives from the entropy of wall breathing: the sizes of the hexagonal domains may be independently adjusted without changing total wall length or number of wall intersections [39]. Adding this entropy term to Bak's zero-temperature mean field theory will decrease Λ for small incommensurabilities, favoring the hexagonal phase over the uniaxial. The model might explain why we see no uniaxial phase, but still rules out any second order transition.

This entropic domain wall interaction produces a very soft structure. The compressibility of the domain

wall lattice approaches zero as the walls move further apart. Coppersmith et al. [40] have estimated the elastic constants of a hexagonal domain wall network, while Nelson and Halperin [14] have calculated the free energy of a free dislocation in a 2D lattice: combining the two results, Coppersmith et al. [40] find that dislocations in the domain wall network have negative free energy, making it unstable and leading to a fluid. Since the elastic constant is due to an entropic term, it decreases linearly with temperature; the result holds for all non-zero temperatures, provided the transition is not too strongly first order.

The Potts lattice gas model used for the C-F transition has been extended by Kardar and Berker [41] to provide a renormalization group treatment of the C-RF transition. While the Potts model assigns one energy for neighboring sites in the same sublattice, another for any combination of different sublattices, Kardar and Berker here use a chiral Potts model, where heavy and superheavy walls (see Fig. 1) and their crossings have different energies. Their renormalization group calculations give a phase diagram for adsorbed monolayers with a fluid phase separating commensurate and incommensurate solids, as in the model of Coppersmith et al. [40]. The helical Potts model predicts a continuous transition, as observed, and provides a heuristic explanation of the one-third power law behavior of the misfit (10).

Since the C-RF and C-F melting transition connect continuously, we must know when the transition falls in the Potts universality class, which has been used to describe the C-F transition, and when it falls in that of the chiral Potts, which applies to the C-RF melting transition. As pointed out by Huse and Fisher [42], the asymmetry between heavy and superheavy domain walls can be either a relevant or irrelevant perturbation to Potts behavior. When it is relevant, the transition will fall in the chiral Potts category everywhere except at one multicritical point. If it is irrelevant, the transition will be of the Potts class when the asymmetry is small, possibly shifting to the chiral Potts class as the asymmetry increases, with a new multicritical point at the crossover. The difference between Potts and chiral Potts transitions should be observable by x-ray diffraction for an appropriately precise measurement: as reduced temperature $t \to 0$, the structure factor scales as

$$S(Q) \sim t^{-\gamma} D(qa/t^{\nu}), \tag{12}$$

where $q = Q - Q_0$ and a is the commensurate phase lattice constant. For the Potts universality class, $D(w)$ has its maximum at $w = 0$, so for incommensurability $\varepsilon \sim t^{\beta}, \beta > \nu$ and $\varepsilon/\kappa \to 0$ as $t \to 0$: the profile broadens more quickly than its center shifts. For the chiral Potts universality class, $D(w)$ is maximum at $w \neq 0$, so $\beta = \nu$ and ε/κ approaches a universal nonzero limit.

Here the comparison of experiment with theory is sketchy. The power-law behavior of (10) applies as a function of temperature as well as chemical potential [8], with the same 1/3 exponent, but the peak width κ has been observed to increase monotonically as the incommensurability decreases; the asymptotic behavior of ε/κ occurs as κ decreases. At the smallest ε, $\varepsilon/\kappa \approx 1$, as one might expect for the chiral Potts model. Prior to this work, the scattering from the F phase had not been observed, so little can be said about the chiral character of the C-F transition.

The picture of the weakly incommensurate phase as a domain wall fluid is supported by molecular dynamics simulations. Using a Lennard-Jones Kr-Kr potential and a sinusoidal Kr-Gr potential, Abraham et al. find a disordered hexagonal array of domain walls, with the walls wandering about while the atoms themselves show little mobility [43]. Thus at a simulation temperature of 97.5 K, the domain walls do not appear to be pinned to the lattice.

IIIB. Sample Preparation and Data Collection

Our sample was a $25 \times 25 \times 3\ \text{mm}^3$ piece of Union Carbide ZYX graphite placed in a beryllium cell of similar dimensions. The large faces of the cell are machined to 0.25 mm thickness to provide x-ray windows. A circular flange on the bottom of the beryllium cell is sealed with an indium o-ring to a copper disk, bolted to the cold finger of an Air Products Displex closed cycle helium refrigerator. A copper spring inside the cell holds the Gr in place.

The refrigerator will cool the sample to 15 K. The cell is surrounded by an aluminized mylar radiation shield cooled to 40 K by the first stage of the two-stage refrigerator. All this is enclosed in a stainless steel vacuum shroud, with a cylindrical beryllium window.

A resistive heater is wrapped around the copper disk below the sample cell; an Air Products temperature controller keeps temperature constant to 0.05 K. Three Air Products silicon diode thermometers are used: one in the temperature control feedback circuit, and one at each end of the cell; these agree to within 0.6 K. Kr (Matheson Research Grade, 99.995% pure) is admitted through a stainless steel tube. While our gas handling system was designed for measuring adsorption isotherms, it is connected to the sample by a 3 m stainless steel bellows: room temperature fluctuations in the large volume of gas in the bellows prevent precise measurement of the quantity adsorbed. Thus we simply keep the sample in equilibrium with an MKS Baratron 1000 Torr manometer and add gas to the

desired pressure. Pressure equilibration is rapid at the high pressures studied: under a minute. The sample was baked in vacuum at 1200 K a week before the experiment and transferred under dry nitrogen into the cell. The base pressure of the Gr, cell, and gas handling system was 10^{-6} Torr.

ZYX is a turbostratic exfoliated Gr; the constituent flakes have large uniform basal planes. The basal planes are preferentially aligned parallel to the large face of the sample; the distribution of tilts is approximately Lorentzian, 8.3° half-width-at-half-maximum (HWHM) [44]. There is no order of the crystallites in-plane. Thus the Bragg rod of a monolayer solid is converted to a cylinder by in-plane powder averaging. Since maximum signal is obtained when sample thickness is close to one absorption length, the sample is oriented so as to scatter in transmission, through the minimum sample thickness. Momentum transfer is in the basal plane, with the basal plane normal also in the scattering plane.

The cryostat is mounted in a 6-circle Huber goniometer, but since the only information is in the longitudinal direction, we used the θ and 2θ circles only to take longitudinal scans. Only the center of the sample is illuminated; the edges are damaged when the sample is cut. The scattering volume is 2 mm high, 5 mm wide, and 2 mm thick; 20 mm^3 of graphite has a surface area of 2000 cm^2 [2], giving a diffracted signal of 11ξ counts/s, where ξ is the overlayer correlation length in Angstroms.

While a Kr monolayer gives a substantial signal, scattering from the Gr substrate, Kr gas, and the sample cell can be larger, so the quality of our data is determined largely by the accuracy of background subtraction. We were able to observe weak fluid scattering not seen in previous experiments because improved temperature control of the SSRL focussing mirror and a more stable synchrotron electron orbit gave a more reproducible background level. We first measured the background due to the Gr alone; by comparing the Gr(002) peak intensity when Kr is added, we determine and correct for the x-ray attenuation due to Kr, both gaseous and adsorbed. Next a scan was taken with 500 Torr of Kr in the cell at 200 K, at which temperature a negligible quantity of Kr is adsorbed. Subtracting the Gr scattering gives the Kr gas contribution, which we subtract from our data after scaling by the gas density.

We find a remaining component of the scattering which we believe is not due to Kr adsorbed on Gr basal planes. This scattering does not change as the Kr monolayer passes through a phase transition, it grows rapidly near the bulk Kr gas-liquid transition, and it is well described by the bulk Kr liquid structure factor, so we attribute it to capillary condensation of liquid Kr and remove it by subtracting a variable amount of this structure factor, determined by neutron scattering [45]. This effect should be reduced by using a more loosely packed form of Gr, such being less susceptible to capillary effects.

Typical values for the scattering subtracted ($T=121$ K, $P=435$ Torr) are 3000 counts/s from diffuse Gr scattering, 770 from Kr gas, and 670 at the structure factor peak of ~ 1.85 $Å^{-1}$ from liquid Kr, compared to a maximum scattering of 5000 counts/s from commensurate Kr at 1.70 $Å^{-1}$; Kr absorbs 21% of the beam. Although the basal planes are for the most part aligned 90° away from our momentum transfer, we see 180,000 counts/sec at 1.875 $Å^{-1}$, the Gr(0002) wavevector, from misaligned crystallites, forcing us to disregard data between 1.85 and 1.90 $Å^{-1}$. More bothersome are three sharp peaks (HWHM ~ 0.006 $Å^{-1}$) in our "clean" Gr background, with wavevectors of 1.7123, 1.7335, and 1.7977 $Å^{-1}$ and intensity ~ 600 counts/s. Both Gr sample and beryllium cell walls are in our scattering volume; we do not know which contains these impurities. Small changes in these peaks, perhaps due to thermal expansion, contribute an uncertainty of ± 100 counts/s to our data at the above wavevectors.

IIIC. Results

The dashed lines in Fig. 3 show the paths through the phase diagram along which we have taken detailed series of diffraction profiles. Representative scans are shown in Figs. 4–8. While these figures show only the vicinity of the Kr(100) peak, in all cases scans were taken and fit from 1.2 to 2.5 $Å^{-1}$ to measure the wings of the peak. Figure 9 shows scans on this broader scale for the three phases; the bulk liquid Kr contribution has not been subtracted and is shown as the dashed line in Fig. 9.

In preparation for this experiment we took much low resolution data using a rotating anode source. For the most part we will discuss only the higher resolution synchrotron results, but low resolution is sufficient for the study of the development of the broad bulk liquid Kr scattering. Figure 10 shows rotating anode scans of a ZYX sample near bulk Kr liquid-gas coexistence. The data are fit to a resolution-limited 2D solid peak and a Kr liquid peak; at high coverage the lineshape can be described by a small amount of 2-D solid and a growing amount of 3-D liquid.

The solid lines in Figs. 4–10 are the results of least squares fits; the best fit parameters are shown in Figs. 11–13 for these and similar scans. To fit the data, we start with a 2-D structure factor $S(|\mathbf{Q}-\mathbf{Q}_0|)$, assumed to be isotropic about the r.l.v. $\mathbf{Q}_0$. As we shall

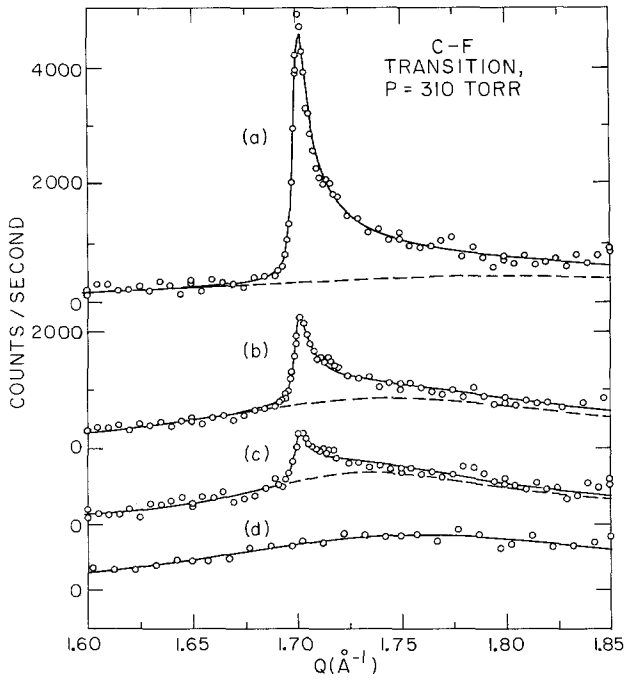

Fig. 4a–d. Powder diffraction profiles, commensurate solid-fluid transition: **a** 127.6 K, **b** 128.75 K, **c** 128.82 K, and **d** 129.5 K. Dashed lines indicate the fluid component of composite lineshapes

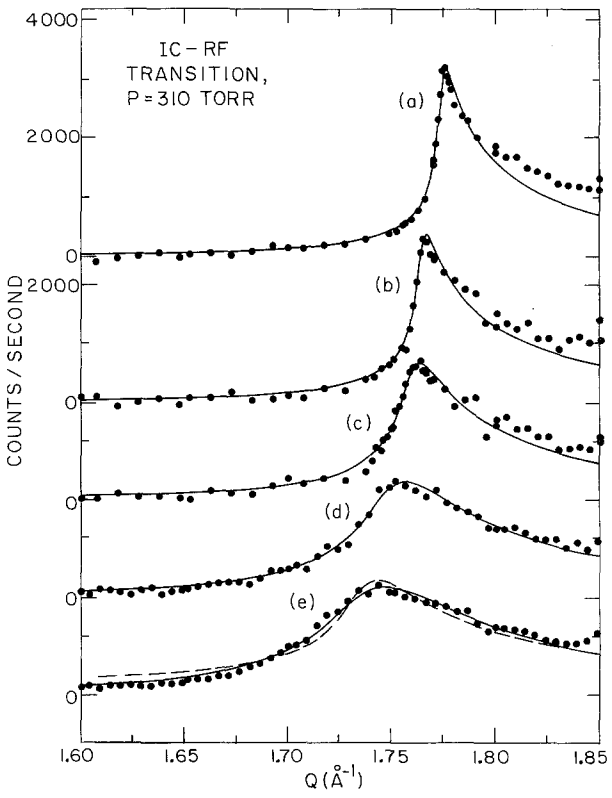

Fig. 6a–e. Powder diffraction profiles, incommensurate solid-reentrant fluid transition: **a** 116 K, **b** 118.5 K, **c** 119.5 K, **d** 121 K, and **e** 122.25 K. Dashed line in **e** is a Lorentzian lineshape, **a** a power law lineshape, the rest follow (16)

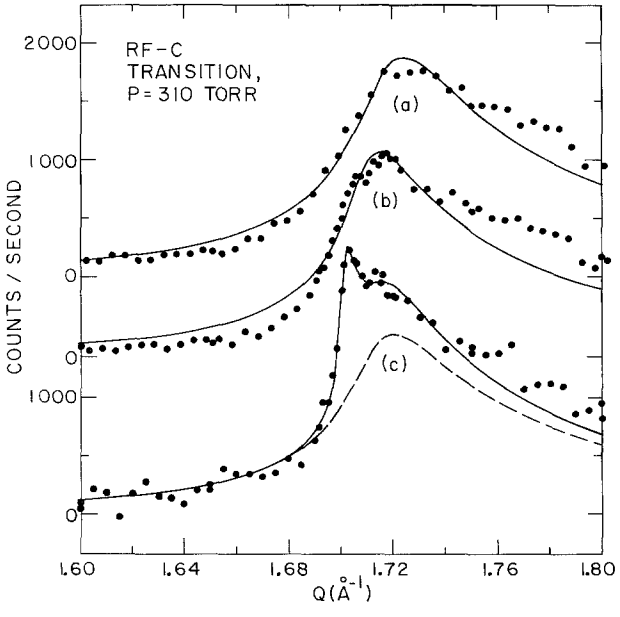

Fig. 5a–c. Powder diffraction profiles, reentrant fluid-commensurate solid transition: **a** 123 K, **b** 123.5 K, and **c** 123.75 K. Dashed line indicates the fluid component of a composite lineshape

see in Sect. IV, this is often the case. The structure factor is then averaged over all in-plane orientations. Finally, the lineshape is averaged over the tilt distribution. Following Stephens et al. [30], the double integral over tilts is converted to a single integral over effective tipping angle. The Lorentzian tilt distribution with 8.3° HWHM is well approximated by a Lorentzian distribution of tipping angles with 15° HWHM.

Instrumental resolution gives only a small correction to the lineshape, so it has been treated in an ad hoc manner: a correction of 0.00079 $Å^{-1}$ is added in quadrature to the HWHM. The data are fit by varying peak width, peak intensity, and peak position. The amplitude of the capillary condensed liquid contribution is determined from the high Q data, $Q \sim 1.90$ to 2.5 $Å^{-1}$, while the Gr scattering, Kr gas scattering, and attenuation due to Kr are fixed as described in Sect. IIIB.

For the commensurate phase, we use the lineshape developed by Stephens et al. [30]:

$$I(q) = A\left[\frac{1.8}{1+q^2/\kappa^2} + e^{-\ln(2)q^2/\kappa^2}\right], \tag{13}$$

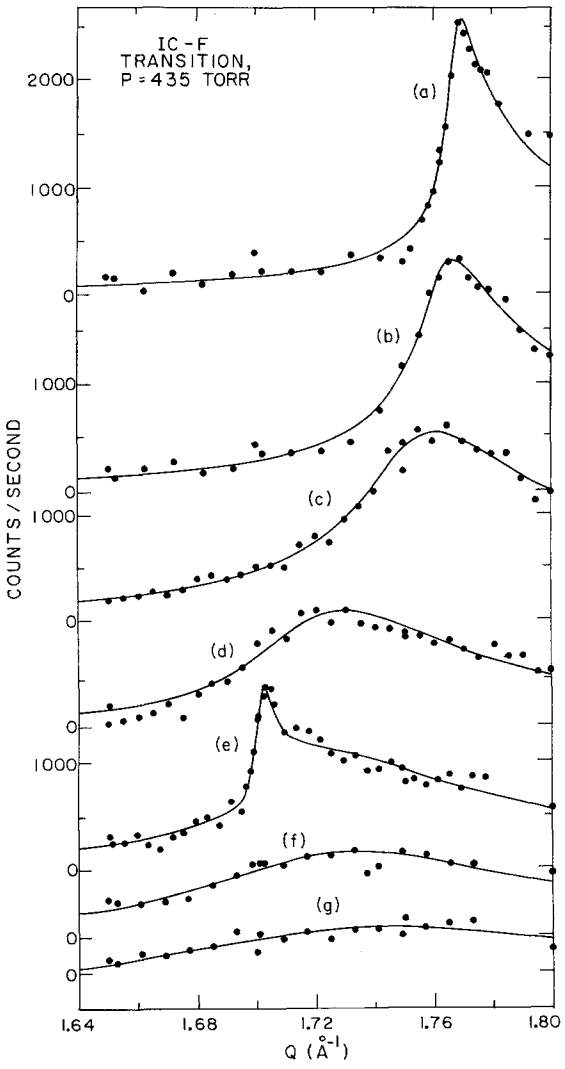

Fig. 7a–g. Powder diffraction profiles, incommensurate solid-fluid transition: a 121 K, b 122 K, c 124 K, d 127 K, e 128 K, f 130 K, and g 132 K

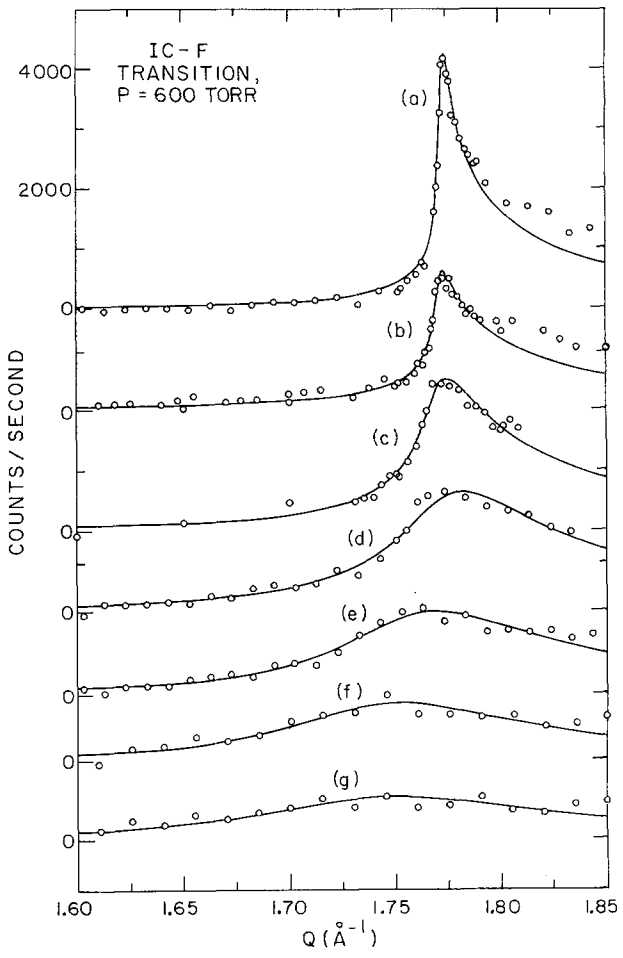

Fig. 8a–g. Powder diffraction profiles incommensurate solid-fluid transition: a 120 K, b 122 K, c 123 K, d 124.5 K, e 127 K, f 130 K, and g 132 K

where $L=2.96/\kappa$ is the domain size. We find $L=1650 \pm 100$ Å, similar to the result of Stephens et al. [30].

As discussed in Sect. 2, the structure factor for a fluid will typically be a Lorentzian spot or a Lorentzian ring. A ring of scattering will be unaffected by powder averaging, but a Lorentzian spot, $S(\mathbf{q}) = \frac{A}{\kappa^2+(\mathbf{Q}-\mathbf{Q}_0)^2}$ will give approximately the square root of a Lorentzian in the powder average:

$$S(Q)=\frac{2\kappa Q_0}{[(\kappa^2+Q^2+Q_0^2)^2-(2QQ_0)^2]^{1/2}} \tag{14}$$

$$\approx \frac{1}{[1+(Q-Q_0)^2/\kappa^2]^{1/2}}, \tag{15}$$

for $Q-Q_0 \sim \kappa \ll Q_0$.

These subtle lineshape distinctions are most readily made in the RF phase: the scattering in the F phase is too broad to permit accurate measurement of the wings of the scattering. Equation (14) gives a poor fit in the RF phase, as shown by the dashed line in Fig. 6e. A Lorentzian ring gives a satisfactory description of the powder data, but as we shall see in Sect. IV, the scattering is a spot and not a ring. We therefore fit the data with yet another lineshape,

$$S(\mathbf{Q})=\frac{A}{1+(\mathbf{Q}-\mathbf{Q}_0)^2/\kappa^2+C_4(\mathbf{Q}-\mathbf{Q}_0)^4/\kappa^4}, \tag{16}$$

which is analytically powder-averaged in-plane. $C_4=0$ gives a Lorentzian spot, $C_4=1/4$ a Lorentzian squared. A fit of (16) to the data with C_4 allowed to vary, yields

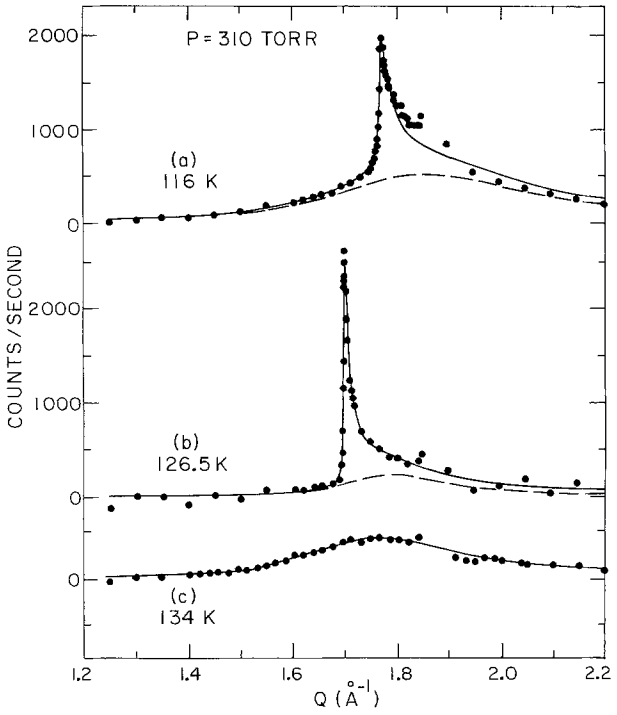

Fig. 9a–c. Powder diffraction profiles on a broader scale. Dashed line in **a** is the bulk liquid component, in **b** the 2D fluid component of the lineshape

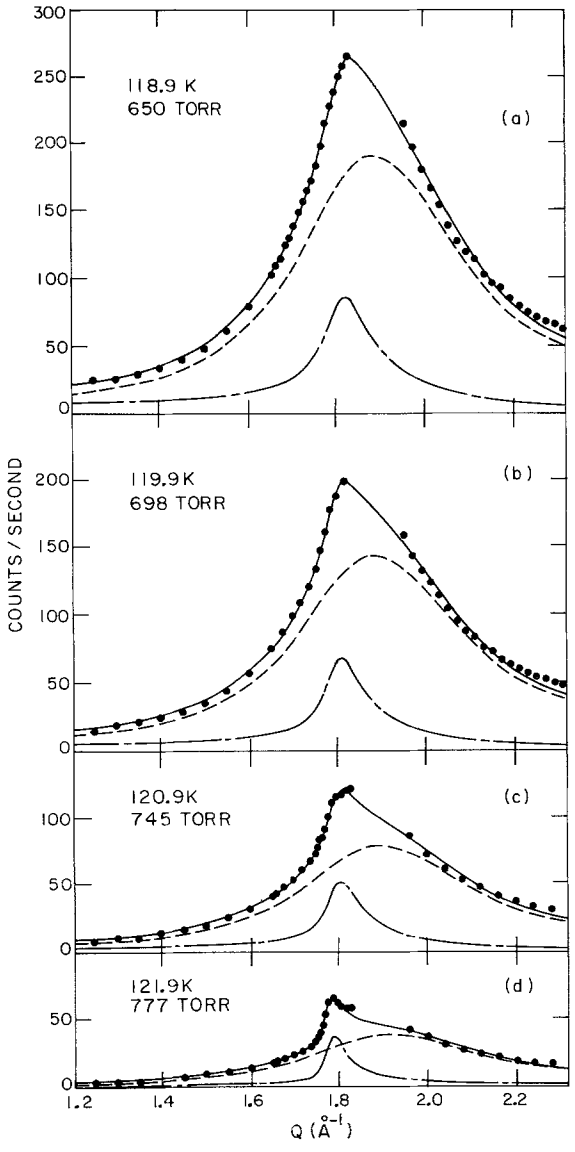

Fig. 10a–d. Rotating anode powder diffraction profiles showing development of bulk liquid scattering. Dashed lines are the bulk liquid component, broken lines that due to the incommensurate solid

values of C_4/κ^2 between 20 and 70 Å^2. To reduce random error in determining the other parameters, C_4/κ^2 is held fixed at 36 Å^2. The Lorentzian lineshape would be expected in the scaling limit, ($q\xi \lesssim 1$). A correction term to a Lorentzian line-shape can be understood for a domain wall fluid, because although correlation distances are large in terms of a unit cell, they are small in units of the domain wall separation.

We would expect the scattering for the IC phase to follow a power-law structure factor (1). Following the procedure of Heiney et al. [46], we can fit our IC lineshapes to the approximation of Dutta and Sinha [47] to a power law lineshape convolved with finite size rounding. However, as found by Heiney et al. [46], the value of η cannot be precisely determined, and indeed a power law lineshape cannot be distinguished from a Lorentzian unless the strength of scattering on the wings of the peak is accurately measured. We cannot determine our Kr gas background accurately enough to do this, so we only demonstrate consistency with a power-law lineshape: the solid line in Fig. 6a is the lineshape developed by Heiney et al. with η set to 1/3, as one might expect near melting [14], and a best-fit finite size of 840 Å. It is reasonable that the finite size found here is smaller than the 1650 Å found in the commensurate phase. Since the IC phase has continuous translational symmetry, its phonon spectrum will have no gap at $\mathbf{q}=0$ and it will be more susceptible to distortion by impurities.

The IC phase may be fit equally well by the lineshape used for the fluid phase, (16). Since we cannot make a clear distinction between fluid and incommensurate solid, and cannot precisely determine η when the scattering is sharp enough to be solid, we fit all the data to this modified Lorentzian lineshape.

Notably absent in all the observed incommensurate lineshapes are the satellite peaks seen at lower temperatures. When the Kr(100) peak is found at

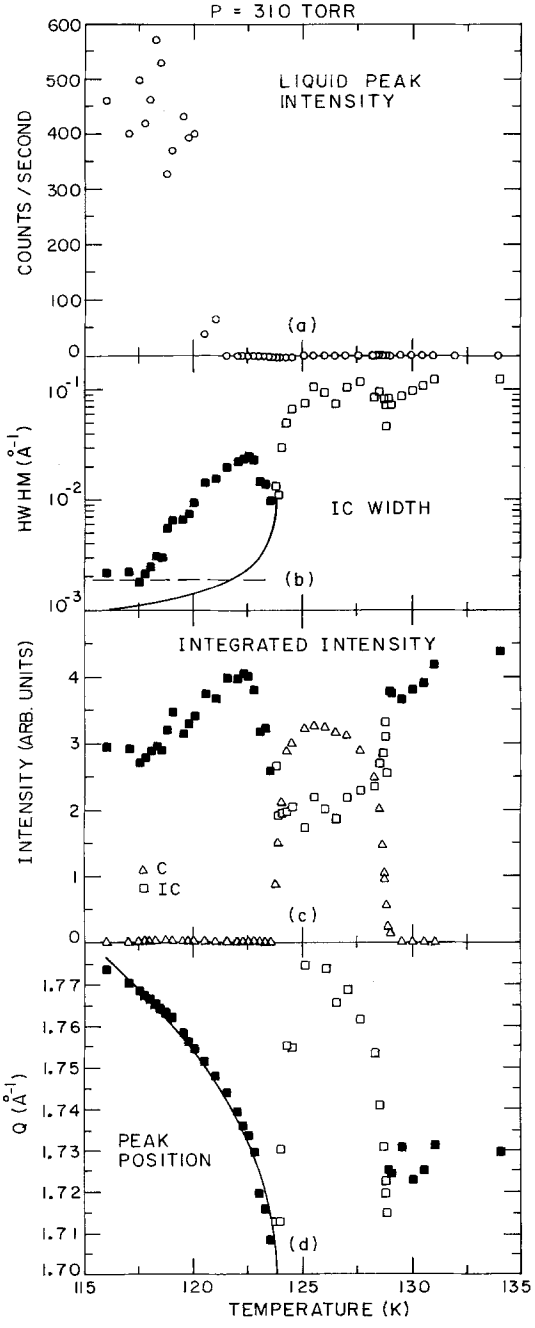

Fig. 11a–d. Best fit parameters, 310 Torr. Solid line in **b** is the estimated contribution of sample inhomogeneity to peak width, the dashed line that of finite domain size. Open squares in **c** and **d** are profiles where the fluid scattering cannot be resolved from the tail of the commensurate peak; these values are unreliable. The solid line in **d** is a power-law fit—see text

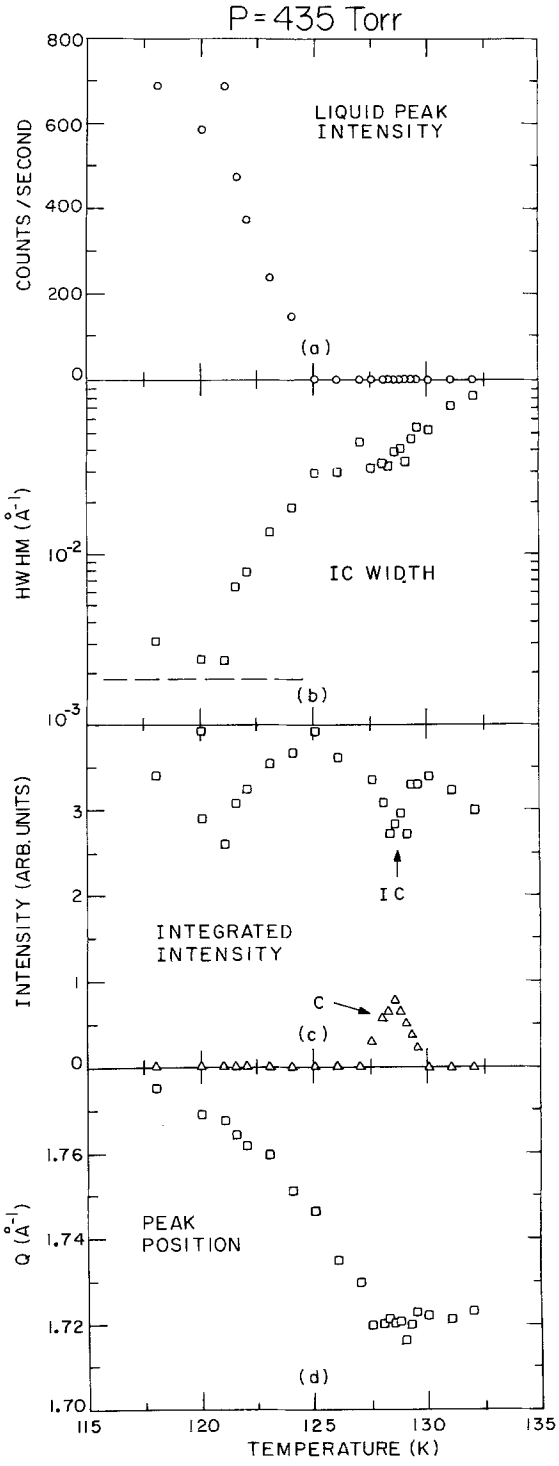

Fig. 12a–d. Best fit parameters, 435 Torr. Dashed line in **b** is contribution of finite domain size to peak width

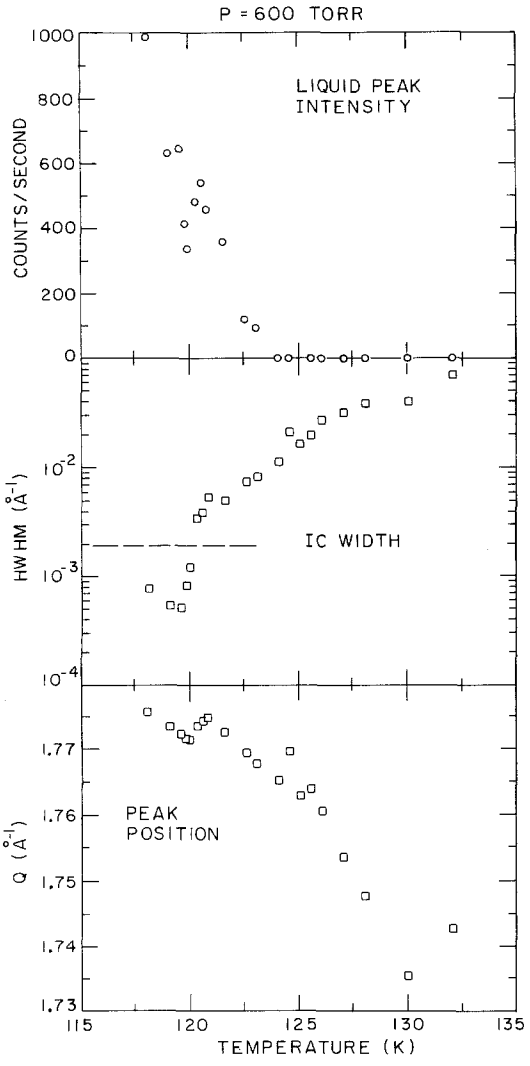

Fig. 13. Best fit parameters, 600 Torr. Dashed line is finite domain size contribution to peak width

$Q_0+\varepsilon$, where Q_0 is the commensurate peak position, the satellite appears at $Q_0-\varepsilon/2$. The incommensurate lineshape will not fit a Lorentzian because it is too weak on this leading edge. Thus it seems unlikely that the satellite peak is present in broadened form.

The existence of a satellite peak can be ruled out only when ε is large enough for the primary and satellite peak to be resolved. From our data around 124 K, we can rule out a satellite peak which is 0.05 as intense as the primary peak for all $\varepsilon > 0.02$ Å^{-1}. In contrast, at 94 K, the relative satellite peak intensity is 0.3 for $\varepsilon = 0.02$ Å^{-1}, and falls to 0.05 only for $\varepsilon = 0.05$ [30]. Thus the satellite peak intensity is at least a factor of six weaker at 124 K, compared with the data at 94 K.

The satellite peak intensity for a disordered system is most easily computed in the limit of an incommensurate solid weakly perturbed by the substrate. To lowest order in the perturbing potential (11), the structure factor is [48]

$$S(\mathbf{Q}) = S_0(\mathbf{Q}) + \sum_{n=1}^{6} (\mathbf{Q}\cdot\delta_n)^2 S_0(\mathbf{Q}+\mathbf{K}_n), \tag{17}$$

where $S_0(\mathbf{Q})$ is the structure factor of the unperturbed overlayer and

$$\delta_n = \frac{\mathbf{K}_n}{9q_0^2 m^2 l_0^2} \tag{18}$$

is the amplitude of the static distortion wave with wavevector $\mathbf{K}_n$ equal to one of the six Gr(100) r.l.v.; $\mathbf{Q}_0$ is the commensurate Kr(100) r.l.v., m the misfit, and l_0 the dimensionless domain wall width.

The first term in (17) gives the primary peaks, unmodified (to first order) by the distortion. The second term gives satellite peaks at $\mathbf{Q} = \mathbf{G}_m - \mathbf{K}_n$, the differences between a Kr and a Gr(100) r.l.v. In the presence of thermal fluctuations in the unperturbed overlayer, the satellite peak will take the intensity and shape of the corresponding Kr peak $\mathbf{G} = \mathbf{Q} + \mathbf{K}_n$. Since the $Q_0 - \varepsilon/2$ satellite peak is the sum of a Gr(100) and a Kr(010) r.l.v., comparing its intensity to the primary Kr(100) gives the displacement δ: *thermal fluctuations drop out*. The satellite peak at $Q_0 + 3\varepsilon/2$ corresponding to a Gr(100) and Kr(200) r.l.v. has not been observed even at low temperatures, presumably because the Kr(200) peak is much weaker than the Kr(100). Since two satellite peaks contribute to the $Q_0 - \varepsilon/2$ peak for each primary peak, the ratio of primary to satellite peak is

$$\frac{S(Q_0-\varepsilon/2)}{S(Q_0+\varepsilon)} = \frac{1}{18}(ml_0)^{-4}. \tag{19}$$

As discussed by Stephens et al. [30], this theory works at temperatures of 94 K and below. In addition, detailed x-ray diffraction studies of the uniaxial system of weakly incommensurate bromine-intercalated graphite verify this scaling of satellite peak lineshape with that of the appropriate principal peak [49].

Both (17) and the bromine intercalated graphite example refer to the modulation of 2D solids; the same argument also applies to a fluid [50, 51, 52]. Thus, simple Debye-Waller type arguments etc. cannot explain the absence of satellite peaks at 124 K. This must instead be due to a change in the width of the domain wall. As the magnitude of fluctuations approaches the wavelength of the modulation of the Kr–Gr potential (2.13 Å), the effective strength of the modulation is reduced as each Kr atom samples an average of the potential. Calculations using the Sine-Gordon equation to model the domain wall structure show that

phonons will increase the width of domain walls in the incommensurate solid by ~60% before the solid melts [53]. In the limit of a weak perturbation, the satellite peak intensity varies as the fourth power of domain wall width (19), so this corresponds to a factor of 0.15 in satellite peak intensity, making the peaks unobservable. A rapid diminution of the satellite peak intensities is also observed in bromine intercalated graphite near melting [49].

Having described the structures observed, we will now consider the phase transitions. The best-fit parameters for the $P=310$ Torr scans are shown in Fig. 11. At the highest temperature, in the F phase, there is a single broad 2D peak (Figs. 4d, 9c). Between 128.5 and 128.9 K, a commensurate peak develops (Fig. 4b, c). As shown by Fig. 11c, the fluid peak does not simply disappear at this point, but becomes weaker by half and shifts to higher r.l.v. (Fig. 11d). Within the C phase the parameters for the fluid component are represented by open rather than filled squares in Fig. 11 to remind the reader that they represent an increased scattering on the tail of the commensurate peak, rather than a resolvable peak: their values are not to be taken too seriously. This is best seen in Fig. 9b, where the dashed line is the incommensurate component of the scattering. This scattering may be thermal diffuse scattering, as suggested by Stephens et al. [30]. Alternatively, it is well described by the liquid bulk Kr lineshape, although this explanation is unappealing because we expect this contribution to increase monotonically as the sample is cooled, and we see no such scattering in the RF phase.

The striking feature of the C-F transition is that we see no evolution of the lineshapes as one would expect near a continuous transition. The scattering is well described by the sum of two lineshapes, with the commensurate peak remaining uniformly sharp as its intensity increases, while the fluid exhibits only a gradual 70% increase in correlation length to ~20 Å in the 2 K interval above the transition. The Kr(100) r.l.v. is a constant 1.73 $Å^{-1}$ to within the 0.01 $Å^{-1}$ experimental resolution in the fluid phase: interpreted naively, this would imply a first order transition with a fluid density 3.6% greater than that of the solid C phase. There is no sign of fluctuations on length scales between 50 and 1000 Å.

Although the Bragg peak intensity rises over a 0.4 K interval, the temperature resolution is somewhat better: even if the correlation length were to diverge from 50 to 1000 Å over 0.1 K, we would see a superposition of lineshapes of different width, rather than a clean sum of a sharp peak and the broad fluid scattering. We can rule out all but an extraordinarily sharp second order transition. We conclude that the transition is strongly first order. While the discontinuity in density must approach zero at a tricritical point, a small jump in density does not imply a weakly first order transition: the density is not the order parameter. A necessary and sufficient condition for the existence of a tricritical point is that the correlation length in the fluid phase at the phase transition diverge approaching the tricritical point: at 310 Torr and 129 K there is little increase in the correlation length as the phase transition is approached from higher temperatures.

We therefore conclude that in this case the growth of the Bragg peak intensity appears to be continuous because of inhomogeneity effects. As noted earlier, the ideally discontinuous changes in coverage and Bragg peak intensity are spread over a larger temperature range than at lower temperatures. This must be due to an increased susceptibility to inhomogeneity, accompanying the increase in fluid density at coexistence. Earlier reports of power-law behavior in Bragg peak intensity and compressibility in fact describe the distribution of inhomogeneity in the system, rather than a second order phase transition. Despite descriptions of tricritical behavior at 117 K and lower, our measurements show that *the transition is first order up to 129* K.

The coexistence line for a first-order phase transition follows the Clausius-Clapeyron formula:

$$\frac{dP}{dT}=\frac{L}{T(v_2-v_1)}, \tag{20}$$

where L is the latent heat, v_2 and v_1 the volume per atom of each phase. Applied to a 2D system, the volumes translate to areas, while the pressure is a 2D spreading pressure. We do not measure this pressure, but whatever the relation between 2D and 3D pressure, the phase boundary has a maximum temperature at 130 K and 400 Torr (Fig. 3). Assuming a smooth phase boundary (no multicritical point), dP/dT diverges at that maximum. Since the latent heat remains finite, the two phases must reach equal density: past that point the fluid will be denser than the solid. Adsorption isotherms have not been measured at such high presures: the large mass in the gas phase makes it difficult to measure small changes in the mass adsorbed. At the maximum temperature of the phase boundary, an adsorption isotherm would exhibit only a change in slope at the phase transition, since the two phases have equal densities but different compressibilities, even for a strongly first order transition. The vanishing of the coverage jump does not imply a continuous transition.

If the magnitude of the wavevector at the fluid scattering peak is taken at face value, the maximum temperature of the phase boundary must occur below

310 Torr, since the fluid is 3.6% denser than the solid. This would require slight modification of the boundary shown in Fig. 3. The fluid is highly disordered, however, so its density need not be that of the solid, scaled by the peak position. Since the commensurate solid forms with an atomic separation some 5% greater than the Kr–Kr potential minimum, it is more likely that the fluid has a first shell at atomic separation 1.8% less than the solid, but contains enough voids to give it a slightly lower density.

On further cooling the commensurate monolayer reenters the fluid phase. We can now see a growth of correlations in the RF phase as it approaches the C phase: HWHM decreases from 0.025 to 0.0097 $Å^{-1}$ before the coexisting C phase obscures the RF scattering, as shown in Fig. 11. This is the reverse of the behavior seen at lower temperatures by Stephens et al. [30], where the correlation length in the RF phase decreased as the ordered C phase was approached. The solid line in Fig. 11b represents the 0.2 K spread in transition temperature multiplied by the derivative of peak position with respect to the temperature: if the transition temperature is spread over 0.2 K by inhomogeneity, this is the peak broadening due to the distribution of misfits. Right at the C-RF transition we see a spread of peak positions comparable to the peak width. Turning to the data in Fig. 5, it is not surprising that a single lineshape gives a poor description of the scattering. Nevertheless, as is evident in Fig. 11b, the increase in width with decreasing temperature is apparent; the measured width in the RF phase is due to equilibrium thermodynamic effects not substrate inhomogeneities.

Plotting peak half-width κ versus incommensurability ε (Fig. 14), we find that roughly $\varepsilon \sim \kappa$ in the region where both are decreasing. In term of a Potts model this implies that the transition falls in the chiral Potts universality class. Inhomogeneity-induced C-RF coexistence spans 0.2 K, while the reentrant melting occurs over a 1 K range, not enough room to extract critical exponents.

At these high temperatures the misfit is well described by an exponent closer to 1/2 rather than the 1/3 observed at lower temperatures. The solid line in Fig. 11d is

$$\frac{Q-Q_0}{Q_0}=0.178[(T_c-T)/T_c]^{1/2}, \tag{21}$$

with a transition temperature $T_c=123.87$. To compare with lower temperature behavior, Fig. 15 shows the incommensurability at constant temperature rather than constant pressure. The dashed line is (10) with the low temperature parameters $A=0.79\%$ and $\beta=1/3$; the solid line is $A=0.58\%$, $\beta=0.44$, the best fit to the data; (21) which has $\beta=1/2$ gives a similar fit. Note that the incommensurability is greater than that extrapolated from low temperatures: this is the opposite of what one might expect for a monolayer. With increasing temperature the disordered RF phase should have a reduced free energy relative to the C phase, and the C-RF transition will occur at a smaller natural misfit.

When the RF finally freezes into the IC phase, the half-width κ approaches zero in the manner expected

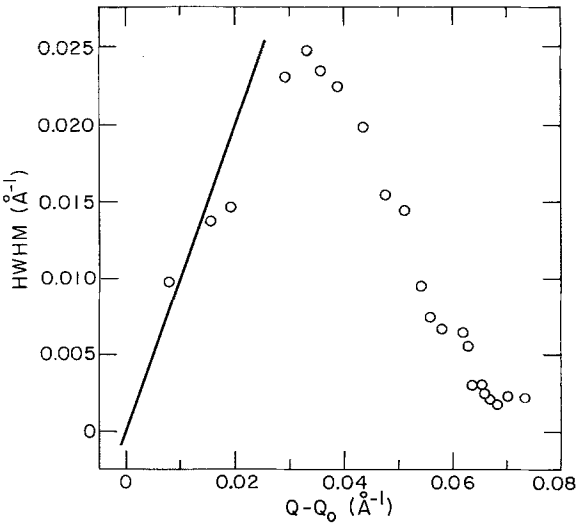

Fig. 14. Peak width versus incommensurability: along the solid line they are equal

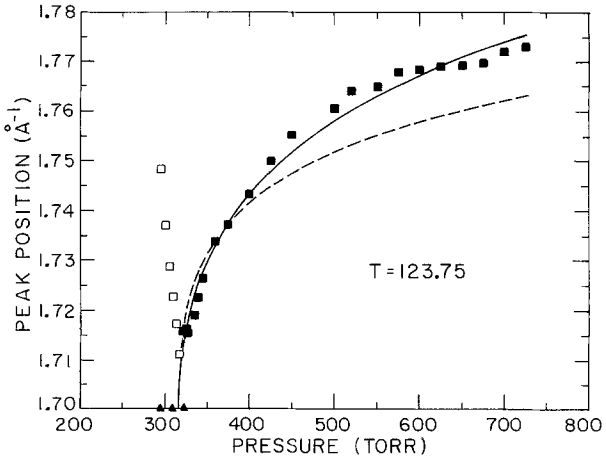

Fig. 15. Reciprocal lattice vector versus pressure: solid line is a 1/2 power law, the dashed line the low temperature behavior (Eq. 10). Triangles are commensurate peaks, open squares fluid peaks which cannot be resolved

for a dislocation-unbinding transition. Close to the C-RF transition, inhomogeneity effects contribute to peak width because the peak position varies rapidly with temperature; near the IC-RF transition the inhomogeneity contribution is important simply because the peak becomes very sharp. To account for this effect as well as finite size effects, we have simply added to the width a constant term equal to the width of the narrowest peak observed, giving

$$\kappa = \kappa_1 + \kappa_0 e^{-B/t^{\nu}}, \tag{22}$$

which is shown in Fig. 16 along with the scaled data. Parameters are $\kappa_0 = 4.11\ \text{Å}^{-1}$, $\kappa_1 = 0.00059\ \text{Å}^{-1}$, $B = 1.8066$, and $\nu = 0.4$; $\nu = 0.37$ gives similar results.

A similar evolution of peak width is seen for the freezing of IC Xe/Gr. However, the transition in the Xe case is much sharper, spanning the same range of correlation lengths in less than 1/30 the reduced temperature [16, 44, 46]. Since the adsorbed atoms are so similar, this suggests that the substrate is playing a strong role in the freezing of the incommensurate overlayer and indeed the freezing mechanisms may be fundamentally different for Kr and Xe. The reduced temperature range over which the correlation length evolves significantly is comparable for monolayer Kr and for the 2D nearest neighbor XY model [54].

Calculations by Joos and Duesbery [55] suggest that while IC Kr/Gr melts by formation of dislocations in a network of domain walls, melting of IC Xe/Gr is a result of dislocations in the atomic lattice. Calculating the energy of dislocation pairs for both systems, they find that due to the anharmonicity of the rare gas interactions, vacancy dislocation dipoles are favored over interstitials for either adsorbate. Since Kr has dense walls, dislocations pinned to the walls are a low energy excitation, while Xe dislocations are repelled by the walls; thus widely separated dislocation dipoles have much lower energy for Kr.

Figure 17 shows how these results fit into the global Kr on Gr phase diagram. Since the 3D pressure has little physical significance for the 2D phases, the plot shows chemical potential, given in temperature units by

$$\mu = T \ln \frac{Ph^3}{kT(2\pi mkT)^{3/2}}. \tag{23}$$

Solid lines indicate first order phase transition, dashed lines second order. Layering transitions are extrapolations from low pressure data [3], assuming they occur at the same fraction of the bulk vapor pressure. The other nearly straight lines are interpolations published

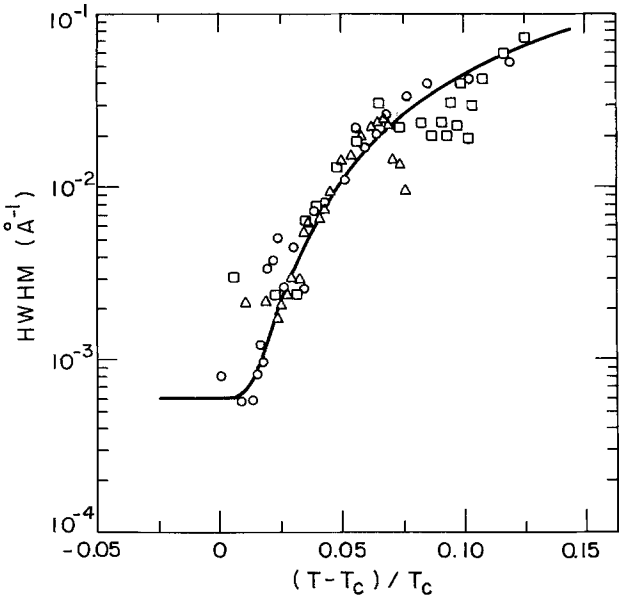

Fig. 16. Peak width through incommensurate melting. Triangles: 310 Torr, $T_c = 114.7$ K; squares: 435 Torr, 117.3 K; circles: 600 Torr, 117.9 K

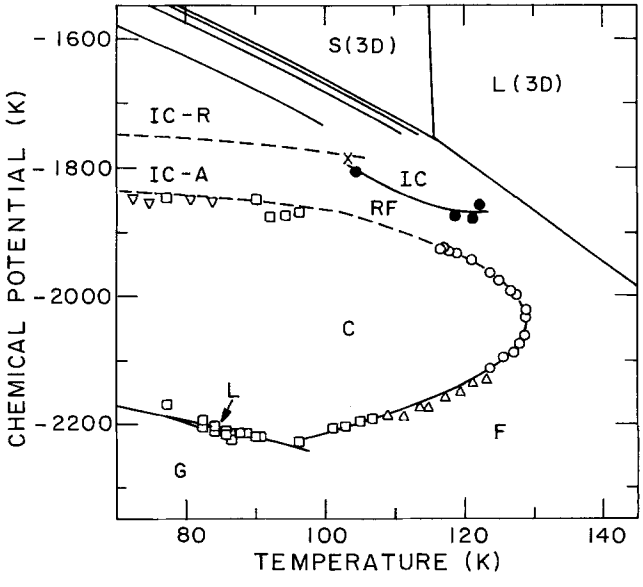

Fig. 17. Kr/Gr phase diagram. Circles this work, triangles [22], squares [4], inverted triangles [6] and [66]. G—gas, L—liquid, F—fluid, C—commensurate, RF—reentrant fluid, IC—incommensurate solid (–A aligned, –R rotated), S(3*D*)—bulk solid, L(3*D*)—bulk Dashed lines are second order, solid lines first order transitions. Lines between IC-R and S(3*D*) are layering transitions, extrapolated from [3]

along with the data shown. The aligned and rotated versions of the incommensurate phase will be discussed in the next section.

Unfortunately, we cannot include on this plot the phase transitions found by Butler et al. [5], who report data as a function of temperature and coverage, rather than temperature and pressure. Comparing topology and correlating temperature between our phase diagrams, they see no IC-RF transition but find a line of phase transitions at 127 to 128 K in our F phase, meeting the C phase at a multicritical point (Fig. 2). A dislocation unbinding transition will give only an essential singularity in the specific heat [14], which may be why Butler et al. see no anomaly at our IC-RF transition. Furthermore, we find that the evolution of correlation is gradual, broadening any specific heat peak still more.

We see no anomaly at what Butler et al. label the IC-F transition. At 600 Torr we see a smooth evolution from the IC to a very disordered fluid (Figs. 8, 13). (The apparent dip in the parameters shown in Fig. 13 is an experimental artifact due to a temporary loss of temperature control.) The C-F and C-RF transitions may be described by a smooth curve,

$$T = T_0 - A(\mu - \mu_0)^2, \tag{24}$$

with $T_0 = 129.08$ K, $\mu_0 = -2042$ K, and $A = 0.000931$, as shown in Fig. 17. This quadratic behavior has been observed in liquid crystal systems [56–58].

The heat capacity peaks identified by Butler et al. [5] as an IC-F transition may correspond to our 435 Torr scan. As shown in Fig. 12c, only a fraction of the overlayer enters the C phase at that pressure. Due to inhomogeneity, some regions of the sample will become commensurate while the rest only approaches the phase boundary, possibly giving the broad, weak heat capacity peak observed by Butler et al. Alternatively, the heat capacity peak may be due to the IC-RF transition, since while there is only an essential singularity at a dislocation unbinding transition, there is a broad heat capacity peak at somewhat higher temperatures [14].

Caflisch et al. [59] have constructed a Potts lattice gas model accounting for both fluctuations in sublattice in the commensurate phase and domain wall fluctuations in the incommensurate phase. Renormalization group calculations give phase boundaries in good quantitative agreement with those given here. They propose another interpretation of the results of Butler et al. [5]. The RF phase, they calculate, occurs at a coverage near 1.1 monolayer. They suggest that what Butler et al. report as a C-IC phase boundary at higher coverage is neither a C-RF nor a RF-IC phase transition but a monolayer-bilayer transition. Since this work has accurately located the C-RF boundary in terms of temperature and pressure, vapor pressure isotherms in this regime would reveal the coverage and settle the issue.

It is clear from Fig. 17 that we cannot claim to have completed the phase diagram. While the C phase is found to terminate at 130 K, we know neither how nor at what temperature the IC phase comes to an end.

IV. Single Crystal Experiments

Structural measurements on single crystal surfaces have traditionally been carried out using electron diffraction techniques. X-ray scattering has a great advantage, however, because photons interact weakly, both with each other and with a sample: multiple scattering is negligible, simplifying data analysis, and highly collimated beams may be produced, providing high resolution. An added advantage for the Kr/Gr system is that we can scatter through high pressures of Kr gas. Here we will present x-ray diffraction measurements using a single crystal substrate which resolve questions which can be answered neither by powder substrate data nor by traditional surface probes.

Scattering from a powder substrate gives no direct evidence of the orientation of the overlayer. Some information may be gained from the lineshape: Dimon et al. [44] find that the scattering from a Xe monolayer on a powder substrate corresponds to a powder-averaged Lorentzian spot near melting, a Lorentzian ring at higher temperatures. This technique is highly dependent on the model used for the lineshape. We make a direct, highly accurate determination of the orientation and structure factor of incommensurate Kr overlayers.

Even for an incommensurate overlayer, which has translational invariance, decoupling it from the substrate, the overlayer is not rotationally invariant with respect to the substrate; thus the underlying order of the substrate is projected onto the overlayer through its orientation. We study this coupling in two ways. For an incommensurate solid overlayer, we see a transition from an aligned to a rotated phase, reflecting the change in the strain produced by the substrate from an array of domain walls to a sinusoidal modulation. By observing small rotations of the overlayer we can determine the strength of the modulations in the substrate-adsorbate potential.

For a disordered, incommensurate overlayer close to the freezing point, we expect to see a hexatic phase with long range orientational order. While the substrate will impose long range order on a highly correlated fluid, an overlayer which would be hexatic with no substrate will have an orientational stiffness,

revealed in a suppression of orientational fluctuations. With a high resolution probe, we can measure orientational fluctuations as the correlation length diverges.

IV. A. Rotational Theory and Previous Experiments

As discussed in Sect. III, when an incommensurate overlayer is subject to a modulated adsorption potential, static distortion waves in the overlayer will form. Novaco and McTague [60] realized that as the overlayer rotates with respect to the substrate, the strain will be taken up in softer transverse modes, lowering the energy.

For a weak corrugation of the Kr-Gr potential (11), the overlayer will respond linearly. For small misfit m and rotation angle θ of the overlayer with respect to the substrate, the energy per atom gained by this strain will be, neglecting higher order terms in m and θ [48],

$$E \approx \frac{-V_0}{12 l_0^2 m^2} \frac{\left(1+\frac{\theta^2}{m^2}\frac{c_L^2}{c_T^2}\right)}{(1+\theta^2/m^2)^2}, \tag{25}$$

where c_L and c_T are the longitudinal and transverse sound speeds.

The strain energy reflects competing effects. The numerator increases with rotation as the strain is accommodated in softer transverse modes, favoring rotation. The denominator increases as the wavelength of the strain decreases. favoring an aligned phase. For $c_L < \sqrt{2} c_T$, the wavelength effect dominates and the overlayer is aligned with the substrate. For $c_L > \sqrt{2} c_T$, the strain energy will be minimum when

$$|\theta| \approx m(1-2c_T^2/c_L^2)^{1/2}. \tag{26}$$

For a hexagonal Cauchy solid $c_L = \sqrt{3} c_T$; the overlayer will rotate by $|\theta| = m/\sqrt{3}$, independent of the magnitudes of the Kr-Kr and Kr-Gr interactions.

This linear response calculation holds when the misfit is small and the corrugation of the Kr-Gr potential still smaller: $1/l_0 \ll m \ll 1$. As the misfit approaches zero and the overlayer strain is accommodated in localized domain walls rather than a sinusoidal displacement, the large commensurate domains between the walls will be strongly held in alignment, since each atom sits at a potential minimum; the low energy modes of rotation will consist of the domain wall network rotating while each domain remains aligned.

In the limit of widely separated domain walls, the problem of overlayer rotation reduces to that of an isolated domain wall. Villain [61] treated domain walls in a pseudoharmonic approximation: the Kr lattice is treated as harmonic everywhere except at a line along the domain wall center, and the sinusoidal corrugation of the Kr-Gr potential (11) is replaced by a second order Taylor expansion about its minimum; this is valid for $m \ll l_0 \ll 1$. Strain falls off exponentially with distance from the domain wall center, giving energy per atom of

$$E \approx V_0 \pi m l_0 \sqrt{3} \left[1+\left(\frac{c_T}{c_L}-\frac{1}{2}\right)\frac{\theta^2}{m^2}\right], \tag{27}$$

neglecting higher order terms as before. Again, the energy of the rotated phase is lowered by the shift of strain to the transverse mode, but raised by the increased domain wall density. The increased density now costs only the energy of an isolated domain wall: interactions are assumed to be negligible.

Note that the angle θ refers to rotation of the Kr(100) r.l.v. about the origin. In fact, each domain wall rotates by a large angle θ/m; each overlayer r.l.v. rotates by θ/m about the nearest commensurate Kr r.l.v. The limit of (26) corresponds to a domain wall rotation of 33°, independent of misfit.

For $c_L/c_T < \sqrt{2}$, the aligned phase is favored in both the linear response limit and the isolated domain wall limit; for $c_L/c_T > 2$ the rotated phase is favored in both limits. The Cauchy solid lies in between, $c_L/c_T = \sqrt{3}$, so it will be aligned with the substrate for small misfit, rotated for large misfit: a phase transition must occur between the two limits. As discussed in Sect. IIIA, Shiba [32, 33] has determined numerically the response of a continuous elastic medium to an external potential. The calculation begins with the linear response approximation discussed above; subsequent iterations account for the variation in potential felt by the medium as it distorts, adding higher harmonics to the distortion. In the limit of small misfit, Shiba's calculation gives a more accurate version of the pseudoharmonic approximation, with the lattice responding harmonically to a sinusoidal potential.

Shiba finds the rotation angle to be a universal function of the misfit, when both are scaled to the wall width parameter l_0. For $c_L/c_T = \sqrt{3}$ the overlayer is aligned with the substrate (i.e. rotated 30°) for $m < m_c \approx 0.7/l_0$, with $|\theta| \sim (m-m_c)^{1/2}$ for $0 < m-m_c \ll 1/l_0$, $|\theta| \approx m/\sqrt{3}$ for $m \gg 1/l_0$.

The domain wall width l_0 may be estimated in a variety of ways which do not depend on orientational information. The Kr-Kr potential is modified slightly due to screening by the Gr substrate, giving an effective Kr-Kr potential well depth of $W \approx 150$ K [62]; theoretical estimates of the corrugation of the Kr-Gr potential range from $V_0 = 4.2$ K [34] to 14 K [35], giving $l_0 = (54 W/V_0)^{1/2}$ between 24 and 42. Shiba

calculates that the commensurate-incommensurate transition occurs at a natural misfit of $1.103/l_0$; using estimates of 4% [29] and 4.5% [63] for the natural misfit gives l_0 of 25 to 28. Satellite peak intensity gives a more direct measurement of domain wall structure: Stephens et al. [30] find a domain wall width corresponding to $l_0 = 38 \pm 7$. Both theoretical and experimental measurements allow considerable latitude, but the critical misfit for rotation would be expected to lie between 1.7% ($l_0 = 42$) and 2.9% ($l_0 = 24$).

At non-zero temperatures, the overlayer orientation will fluctuate. If the potential minimum is $\theta = 0$, we will see the behavior discussed in Sect. IIA, (7) and (9). The lattice in the problem will be a lattice of domain walls in the limit $ml_0 \ll 1$, the atomic lattice in the limit $ml_0 \gg 1$. For a nonzero rotation, there may be more complex behavior. A solid or hexatic phase has long range orientational order, so at low temperature an overlayer will rotate coherently. With increasing temperature fluctuations about the equilibrium rotation will increase. In the simple picture the orientationally disordered overlayer is composed of domains each rotated by the same angle clockwise or counterclockwise and the transition will fall in the 2D Ising universality class.

Electron diffraction experiments suggest a continuous transition from an aligned to a rotated phase with increasing incommensurability [29, 64]. Poor instrumental resolution hindered observations near the transition; what was actually seen was a transition from a circular spot to one elongated in the transverse direction. Only for the largest misfits could the clockwise and counter-clockwise rotated domains be resolved. If a single rotation angle is assumed (plus or minus), the transverse broading indicates a critical misfit near 2% [29], as expected. Measurements of the magnitude of the misfit from different experiments are in disagreement. Although both studies used flakes of natural graphite at temperatures near 50 K, one found a rotation of 0.5°, the other one of 1.2°, both at the saturated misfit of 5%. A history-dependence of the rotation seems the likely explanation; neither experiment determines the reversibility of the rotation. For this relativity large misfit the linear response approximation may be accurate: $|\theta| = m/\sqrt{3} = \pm 1.7°$.

The electron diffraction results are resolution-limited in the longitudinal direction throughout the incommensurate phases, implying positional order and justifying the ansatz of orientational order. However, higher resolution x-ray diffraction studies using a powder substrate found the weakly incommensurate phase to be longitudinally broadened, providing no direct information about the overlayer orientation, but suggesting that the electron diffraction results need to be re-examined; specifically, in a disordered phase, transversely broadened spots could be the result of rotational fluctuations, rather than coexistence between two orientationally ordered rotated phases. By performing high-resolution x-ray diffraction on a single crystal of Gr we combine the critical elements of both experiments, to answer two questions: is the overlayer solid or fluid at the critical misfit for rotation, and does the overlayer rotate coherently, or is the rotation preceded by orientational fluctuations?

IV.B. Sample Preparation and Data Collection

We report two experiments using single crystal graphite substrates. In the first, conducted at SSRL, we measured the transition of the incommensurate krypton overlayer from an aligned to a rotated phase. In the second, conducted at NSLS, we measured the magnitude of the orientational fluctuations in the reentrant fluid.

The SSRL experiment used a natural graphite crystal, the NSLS experiment a synthetic Kish crystal. Both were about 2×3 mm^2 in area and were cleaved to expose a clean face. The SSRL sample was much thinner: 0.025 mm versus 0.25 mm but had a somewhat larger macroscopic bend.

The sample, pinched between tantalum clips, is mounted in a cylindrical beryllium cell. The crystal is cleaned in situ by passing current between the Ta clips, across the sample, heating it resistively. Current is increased until the temperature of a *W*5%*Re*/*W*26%*Re* thermocouple spot-welded to one of the Ta clips reaches 900°C; the graphite crystal will be much hotter. The SSRL sample was secured at two points, holding it more securely but introducing stress.

For the NSLS experiment, we included in the cell a 0.25 cm^3 Teflon frame closed with Be windows and filled with vermicular graphite. When operating at Kr pressures too low to measure conveniently, we can put enough gas into the cell to produce the desired coverage on the vermicular graphite; the single crystal will then equilibrate at the same coverage. The experiments described here were conducted at relatively high pressures. Pressure was measured using a 100 Torr MKS capacitance manometer, but coverage could not be measured, due to room temperature fluctuations.

The vermicular graphite also serves as a buffer. During the SSRL experiment, where vermicular graphite was not used, fluctuations in room temperature led to uncontrolled pressure fluctuations. Accordingly, the cell was sealed off from the gas handling system to reduce the problem; this, however, meant that we could not measure pressure as temperature was varied. In the NSLS experiment, as room temperature and therefore

gas pressure increase, the vermicular graphite, held at constant temperature, adsorbs more krypton, lessening the pressure increase. The Be windows on the vermicular graphite container allow scattering from the vermicular as well as the single crystal. The vermicular was baked under vacuum at 900°C and transferred to the cell under dry nitrogen.

The cell was mounted on a Displex closed cycle helium gas refrigerator, as in the *ZYX* experiment. Air Products platinum resistance (NSLS) or silicon diode (SSRL) thermometers were used to control and measure cell temperature. While the temperature of the measurement thermometer was well controlled, the sample temperature and pressure were not so stable; counting times were limited by drifts in lattice constant. In the SSRL experiment these correlated with pressure fluctuations induced by changes in room temperature. The addition of the vermicular graphite ballast for the NSLS experiment eliminated this effect, but lattice constant fluctuations corresponding to a 0.3 K temperature change remained. We do not fully understand the source of these apparent fluctuations. They are not present in our more recent experiments.

Since a graphite single crystal is more exposed to impurities than a *ZYX* sample, we took greater care to keep this system clean. Gas is admitted to the cell through a 1/4″ stainless steel tube and bellows 12″ long, leading out of the cryostat. The balance of the system is connected with 3/4″ stainless steel tubing, joined by Conflat flanges, including a 1 m long bellows to allow motion of the cryostat, which is mounted on a 6-circle goniometer. The components external to the cryostat were baked to 200°C, the sample cell itself to only 100°C, as it was sealed with indium. Base pressure was 10^{-7} Torr outside the cryostat. At low temperatures, the base pressure within the cryostat was much smaller.

The outgassing rate from the sample cell is 1.0×10^{-7} Torr-l/s while the cell is under vacuum at room temperature; during the experiment, the cell is cool so that the actual outgassing rate is much lower. Even at room temperature, the pressure increase when the cell is sealed off saturates, that is, the level of gas impurities reaches an equilibrium value. Thus our only reliable measure of gas purity is our sample lifetime: every few days we observed a sudden broadening of the incommensurate peaks we were studying; the commensurate Kr peak remained sharp but lost a factor of two in intensity. The scattering could be returned to its original form by flash-heating, warming the sample cell to room temperature and admitting fresh gas.

The Gr crystals were selected based on detailed study of their bulk mosaic, which may be carried out at high resolution using a rotating anode source. Characterization of the graphite surface was possible only using the synchrotron source. The crystals have both a discrete mosaic corresponding to grain boundaries and a continuous mosaic corresponding to elastic deformation. Since the thin flakes are flexible in the out of plane direction, we see a more continuous mosaic in that direction, with one (NSLS) or two (SSRL) crystallites and a mosaic of $\sim 0.4°$ HWHM. Within the basal planes the graphite exhibits more grain boundaries. The NSLS sample is comprised of five crystallites at relative angles of 0°, 0.8°, 5.1°, 5.5°, and 9.9°, with relative intensities of 0.02, 1, 0.4, 0.09, and 0.01; typical width is 0.07° HWHM.

A wide variety of probes was available to characterize the graphite basal plane surfaces, but none match the resolution with which we analyze the Kr overlayers. We therefore determine the quality of the surfaces of our crystal by growing a commensurate Kr monolayer and measuring its mosaic and coherence length. The commensurate overlayer is aligned with the substrate, so we obtain an accurate measure of the surface mosaic. The coherence length of the overlayer may reflect either the distance between steps on the surface or the effect of point defects or impurities which pin the phase of the overlayer.

The in-plane mosaic of the commensurate Kr overlayer is similar to that of the substrate. The most intense peak has a width of 0.07° (SSRL) or 0.025° (NSLS), with weaker peaks extending over 1°. Both the coherence length and out-of-plane mosaic are found from a radial scan through the commensurate overlayer peak [65]; out-of-plane mosaic is 1.4° (SSRL) or 0.4° (NSLS), while the radial width is limited by our 3×10^{-4} Å^{-1} instrumental resolution, implying a coherence length of at least 10,000 Å.

We orient the krypton overlayer by aligning our resolution function with the overlayer Bragg rod. When the graphite surface is aligned with the scattering plane, the Bragg rod lies in the direction of poorest resolution, and scattering is maximum. Having thus levelled the basal planes, we can once again use our diffractometer as a two-circle instrument. When the sample is flash cleaned it rotates by a few hundredths of a degree in-plane, so the crystal axes must be redefined; this was done by finding the commensurate phase peak. At each temperature point, the Kr(100) peak was located, and a longitudinal and a transverse angular scan taken through the peak. This was difficult when pressure or temperature was fluctuating, since the incommensurate peak position changes concomitantly.

Counting rates at NSLS were $5 \times 10^{-5} \xi^2 s^{-1}$, where ξ is the overlayer correlation length in Angstroms. For the one scan with the weakest correlations, we increased this rate by replacing the Ge(111) analyzer with a pyrolytic Gr(002) analyzer. Its angular acceptance is limited by slits to 0.11°; the mosaic of the

crystal was 0.50°. This increases the signal by a factor of 60.

IV.C. Results

The SSRL experiment was the first to study rare gas overlayers on a single crystal of graphite using high-resolution x-ray diffraction [10]. As might be expected, it proved easier to determine reciprocal lattice vectors than to study lineshapes, so we first studied the transition of incommensurate Kr from aligned to rotated. Following the same course, we will defer a detailed examination of the weakly incommensurate Kr fluid and begin by discussing the orientation of incommensurate Kr.

Our results consist of one cut through the phase diagram. The sample cell was sealed off from the gas handling system at 91 K and 2.2 Torr. Since the sample cell contained only a single crystal of graphite, we expect that little Kr adsorbed as the cell was cooled to 72 K, so pressure would drop to 1.7 Torr, following the ideal gas law. Figures 18 and 19 show longitudinal and transverse scans through the Kr(100) peak as the sample is cooled.

The first scan is taken in the commensurate phase. The longitudinal width is resolution limited, while the transverse width reflects the mosaic of the substrate.

The solid lines in Fig. 19 are the results of least squares fits to a sum of Lorentzians. The lines in Fig. 18 are a somewhat more complex model. The structure factor is assumed to be isotropic and Lorentzian; this lineshape is convolved analytically with a Lorentzian in-plane mosaic and numerically with a Lorentzian out-of-plane mosaic. The out-of-plane mosaic was found to be 1.5° in the commensurate phase, and was held fixed at this value for the other scans.

For small angles, the angular average over a mosaic of width $\Delta\theta$ may be approximated by an average in the transverse direction of width $G\Delta\theta$. For a structure factor

$$S(\mathbf{Q})=\frac{A}{\kappa^2+(\mathbf{Q}-\mathbf{Q}_0)^2} \tag{28}$$

convolved with an in-plane mosaic

$$M(q_\perp)\approx\frac{1/G\Delta\theta}{1+q_\perp^2/(G\Delta\theta)^2}, \tag{29}$$

the scattering will be

$$I(\mathbf{q})=\frac{A}{[\kappa^2+q_{||}^2+G\Delta\theta(\kappa^2+q_{||}^2)^{1/2}]\{1+q_\perp^2/[(\kappa^2+q_{||}^2)^{1/2}+G\Delta\theta]^2\}}. \tag{30}$$

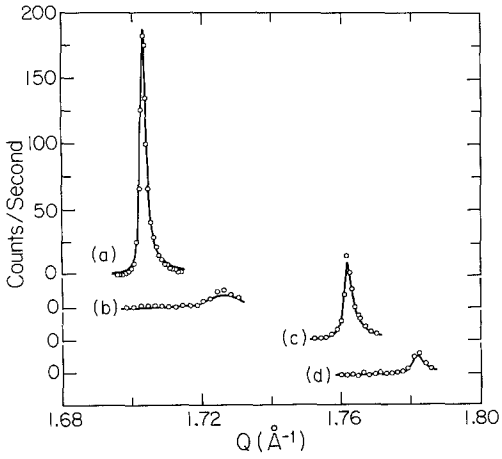

Fig. 18a–d. Longitudinal scans, $P\sim 2$ Torr: **a** commensurate phase, 94 K, **b** incommensurate aligned, 90.65 K, **c** incommensurate aligned, 83.5 K, and **d** incommensurate rotated, 75 K

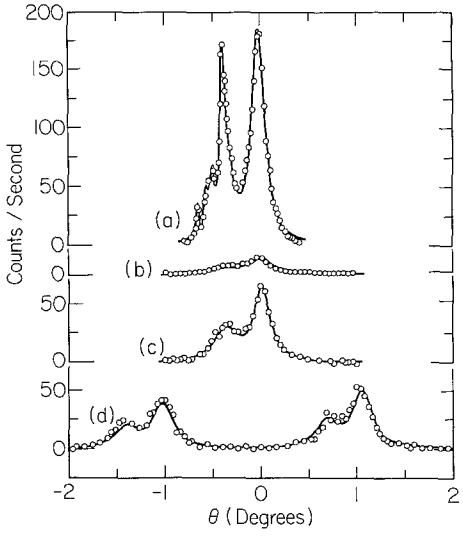

Fig. 19a–d. Transverse scans, $P\sim 2$ Torr: **a** C phase, 94 K, **b** IC-A, 90.65 K, **c** IC-A, 83.5 K, and **d** IC-R, 75 K

where $\mathbf{q}=\mathbf{Q}-\mathbf{G}$. For a simple Lorentzian mosaic, $q_\perp=0$ for a longitudinal scan, giving

$$I(q_{||})=\frac{A}{\kappa^2+q_{||}^2+G\Delta\theta(\kappa^2+q_{||}^2)^{1/2}}, \tag{31}$$

which crosses over from a Lorentzian for $q_{||}\gg G\Delta\theta$ to the square root of a Lorentzian for $q_{||}\ll G\Delta\theta$. The

actual mosaic is a sum of Lorentzians, so only one of several $q_\perp$ is zero for a longitudinal scan. The transverse scan remains a sum of Lorentzians however: for $q_{||}=0$,

$$I(q_\perp)=\frac{A(1+G\Delta\theta/\kappa)}{(\kappa+G\Delta\theta)^2+q_\perp^2}; \tag{32}$$

the widths of the mosaic and structure factor simply add in the transverse scan.

Both longitudinal and transverse scans are fit to (30); the width of the transverse scan is the sum of an isotropic width κ and two mosaics $G\Delta\theta$, one due to substrate mosaic which is fixed to the lineshape of Fig. 19a, the other varied to reflect rotation of the overlayer. The width of the longitudinal scan reflects all three factors mixed together: only by fitting both scans together can both κ and $G\Delta\theta$ be extracted.

Longitudinal and transverse scan in Figs. 18b and 19b show a weakly incommensurate overlayer, misfit of 1.4%. While the peak is less intense and longitudinally broadened, this is primarily an experimental artifact: the longitudinal width is 0.0044 Å^{-1} HWHM, but the thermal expansion coefficient is 0.05 $\text{Å}^{-1}/\text{K}$, and the commensurate and incommensurate phases coexist over a 0.1 K range, so the longitudinal width is in large part due to inhomogeneity effects. Similar results at the C-RF transition were found in the ZYX graphite experiments discussed in the previous section. Consistent with this inhomogeneity explanation, there is no appreciable transverse broadening: the solid line through the transverse scan (Fig. 19b) is the same shape as that through the incommensurate solid lineshapes (Fig. 19c, d). Since the reentrant fluid phase is difficult to measure here due to substrate inhomogeneity effects, our subsequent experiment at NSLS examined higher temperatures and pressures, where the fluid correlations are shorter range; the narrower mosaic of the crystal used in the NSLS experiment also improved resolution. The 0.1 K temperature spread of the transition is an unpleasant surprise; we had hoped that a graphite single crystal would provide much greater homogeneity than our powder samples, but such was not the case. Certainly we can rule out a 0.1 K temperature gradient on our small crystal.

As incommensurability increases the thermal expansion coefficient is reduced; the longitudinal scan in Fig. 18c, taken at 3.5% misfit, exhibits the 0.0011 Å^{-1} HWHM characteristic of the IC solid phase. Taking the 5×10^{-4} Å^{-1} width of the C phase as a measure of instrumental resolution and finite size effects, the intrinsic width of the IC peak is 6×10^{-4} Å^{-1}. Since some of this width is due to the power-law lineshape rather than a finite length [46], the coherence length of the IC phase is close or perhaps equal to that of the C phase.

The transverse scan (Fig. 19c) exhibits broadening as well. This is easy to observe but difficult to measure accurately: the fine structure seen in the C phase (Fig. 19a) simply disappears, leaving two peaks which are only slightly broader than those of the C phase. Considering the large peak at $\theta=0$, the peak broadens from 0.077° HWHM in the C phase to 0.097° in the IC phase, an increase of $G\Delta\theta=6\times10^{-4}$ Å^{-1}. Thus the spot is circular, suggesting no orientational fluctuations. We will discuss this further after presenting similar data for the RF phase.

Figures 18d and 19d show the rotated phase, at a misfit of 4.6%. The solid lines in the figures are simply the fits to the aligned phase (Figs. 18c, 19c) shifted longitudinally and duplicated with $\pm\theta$ rotation. The shape of the peak does not change as the overlayer rotates. The intensities must be adjusted in an ad hoc manner, as the two rotated phases have slightly different intensities.

Figure 20 is a plot of rotation angle θ as a function of misfit. Figure 20a shows Kr data for the present work, as well as a single point from [64]; since Kr saturates at 5% misfit we also show electron diffraction data for Ar at higher misfit [66]. The dashed line is the linear response limit (26) for a Cauchy solid; since the angle of rotation is independent of the magnitude of the adsorbate-adsorbate or adsorbate-substrate forces, we

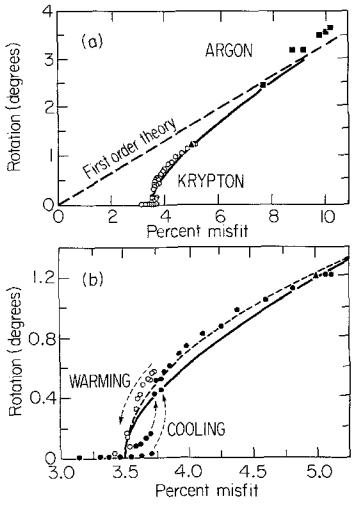

Fig. 20a and b. Rotation data for temperatures from 70 to 85 K: **a** misfit vs. rotation angle for Kr from present work (circles) and [64] (triangle), and for Ar (squares) from [66]. Dashed line is the Novaco-McTague prediction for a Cauchy solid. Solid curve is Shiba's prediction scaled to a critical misfit of 3.5%. **b** is the same data, shown on an expanded scale to illustrate hysteresis. The dashed curve is a power law $\theta\sim(m-m_0)^{1/2}$

treat the Kr and Ar systems together as Cauchy solids, with no free parameter in this model.

The solid line in Fig. 20a and b is the result of Shiba's calculation, which includes the domain wall corrections necessary at smaller misfit [33]. Again fixing the ratio of longitudinal to transverse sound speed at $\sqrt{3}$, we have one free parameter, the domain wall width l_0, which is set to 20 to agree with the critical misfit of 3.5%. This falls slightly below other estimates of l_0, which range from 24 to 42 (Sect. IVA). The theoretical curve describes the data well except near the transition, where we observe hysteresis. Adjusting the second parameter in the theory, the ratio of sound speeds, would presumably improve the fit, but the theoretical curve is published for only the single value of $\sqrt{3}$; in any case we expect only small deviations from this Cauchy behavior.

The dashed curve in Fig. 20b is the mean field power-law, $\theta = A(m - m_c)^{1/2}$, which is the asymptotic form of the solid curve. This form provides a better description of the data, albeit with one more free parameter. This form does not have the advantage of approaching the asymptote of the first order theory. Similar power law behavior has been seen for the orientation angle in $C_{24}Cs$ [67].

Hysteresis typically occurs at a first order transition. However, within the hysteresis loop at the aligned-rotated transition we see a continuous evolution of the rotation angle, rather than three-phase coexistence between the aligned, clockwise, and counterclockwise rotated phases. We can thus rule out any first-order jump in angle greater than 0.2°.

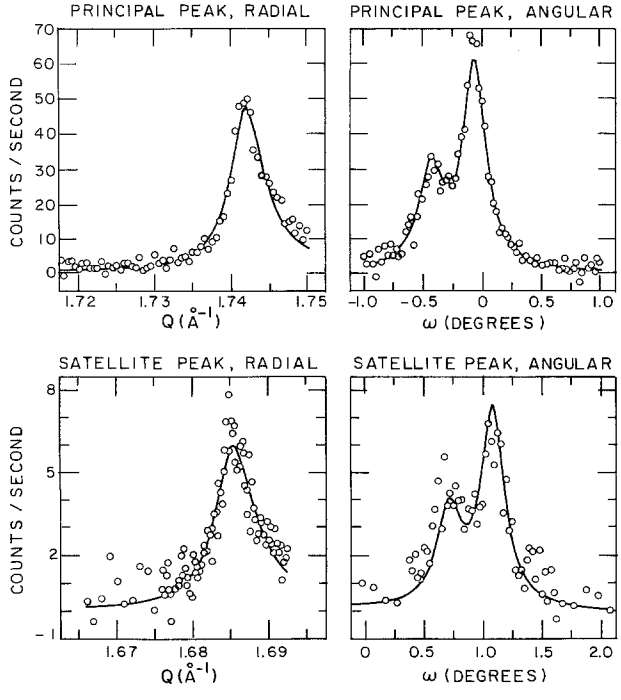

Fig. 21. Diffraction profiles of principal (Kr(100)) and satellite (Kr(010)+Gr(1000)) peaks

The mechanism for hysteresis may be inhibited equilibration due to pinning of domain walls. Here the domain walls are part of the equilibrium structure rather than the result of defects. Sharp domain walls might be pinned by the graphite lattice itself, but here it is more likely that they are pinned by impurities and Gr lattice defects.

An increased hysteresis would explain the results of Fain et al. [6]. Working at a much lower temperature (52 K), they observe rotations about half as great at each misfit. Since these measurements were taken with increasing Kr pressure, the difference could reflect a large hysteresis at lower temperatures. Since the critical misfit found by Fain et al. [6] is closer to zero-temperature estimates, the 3.5% critical misfit observed in this work may be an equilibrium effect of non-zero temperature.

As an independent measure of domain wall width, we measured satellite peak intensity. At a misfit of 2.2%, the principal peak is 8.5 times as intense as the satellite peak, but with the same shape (Fig. 21). Since the aligned-rotated transition corresponds to the crossover from isolated domain walls, which are aligned with the substrate, to a sinusoidally modulated overlayer, which rotates, we calculate satellite peak intensities using a model which includes both limits. We begin with a hexagonal lattice with misfit of 1/44; since this is a commensurate structure it is no longer translationally invariant and we must choose its position relative to the substrate. For convenience we consider a lattice where a sublattice of atoms 108 Å apart lie at the centers of graphite hexagons. The lattice is aligned with the substrate. In the limit of sharp domain walls, this corresponds to the structure shown in Fig. 1c. In our calculation we gradually turn on a sinusoidal Kr-Gr potential (11) while nearest neighbor Kr atoms interact harmonically. With each increase in potential, the Kr atoms are allowed to relax to their equilibrium positions.

This is done iteratively. For each iteration, each Kr atom is moved to the minimum of the potential due to the substrate and its six neighbors, using their positions in the previous iteration. The sinusoidal Kr-Gr potential is approximated by a quadratic Taylor expansion at each Kr position, so the potential minimum may be found analytically. As the computation converges, this approximation becomes increasingly accurate. The process is continued until the root mean square displacement from the previous iteration is less than 10^{-6} Å. For each value of the potential the structure

factor is computed at the Kr(100) and satellite peak positions.

The calculation has two free parameters, the minimum energy Kr-Kr separation, fixed at $r_0 = 4.04$ Å, and the ratio of the Kr-Kr and Kr-Gr potential energies, which is varied. Thus the Kr-Gr potential is

$$V(\mathbf{R}) = -\sum_{i=1}^{3} V_0 \cos(\mathbf{K}_i \cdot \mathbf{R}), \tag{33}$$

the Kr-Kr potential

$$U(r) = \frac{2}{3} V_0 l_0^2 \left(\frac{r}{r_0} - 1\right)^2; \tag{34}$$

V_0 drops out of the calculation, and l_0 is the domain wall width parameter.

The simulation is first equilibrated at $l_0 = 100$, giving a hexagonal lattice with a weak sinusoidal modulation. l_0 is decreased one unit at a time, with the system equilibrated at each step; the principal and satellite peak intensities are shown in Fig. 22. For high l_0 the satellite peak intensity follows (19), while as $l_0 \to 0$, the structure approaches that of Fig. 1c, with comparable principal and satellite peak intensities.

The measured intensity ratio of 8.5 corresponds to wall width $l_0 = 25$, close to the $l_0 = 20$ found from the critical misfit for rotation. Figure 2 of Ref. 53 depicts such a relaxed domain wall. Displacements from the commensurate sites are small outside the domain walls; Figure 23 shows the displacement of each atom in a column extending from a domain center to a domain wall crossing. The solid line is the strain for a uniaxial array of walls in the pseudoharmonic approximation discussed in Sect. IVA [61]:

$$D = A \sinh(n/\lambda), \tag{35}$$

where n is the row of the atom. As expected, this describes the data well except near the wall center, but λ is modified by the hexagonal domain wall lattice: we expect $\lambda = \sqrt{2 l_0}/3\pi = 3.75$ for a uniaxial array, but observe $\lambda = 2.44$ in the simulation.

Similar calculations have been carried out for other domain wall structures. Gooding et al. [36] use the same method to calculate structures for superlattices with a variety of lattice constants and both heavy and superheavy domain walls. By working in reciprocal rather than real space, Shiba [32, 33] calculated structures for truly incommensurate lattices.

We see that disorder plays a small role in the transition between aligned and rotated phases. While the Bragg peaks in the incommensurate phase are slightly broader than those of the commensurate phase, due to an unknown combination of quenched disorder and thermal fluctuations, there is no change in their width through the rotation transition. The variation of overlayer orientation as a function of lattice

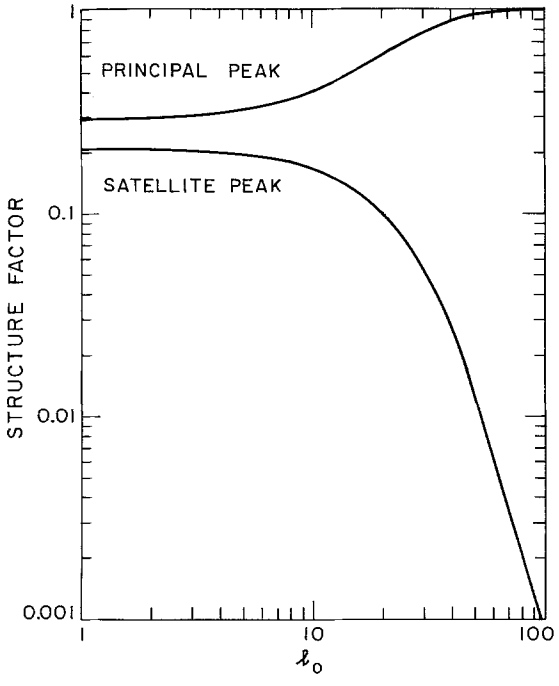

Fig. 22. Calculated intensity of principal and satellite peaks for a misfit of 2.27% as a function of domain wall width parameter

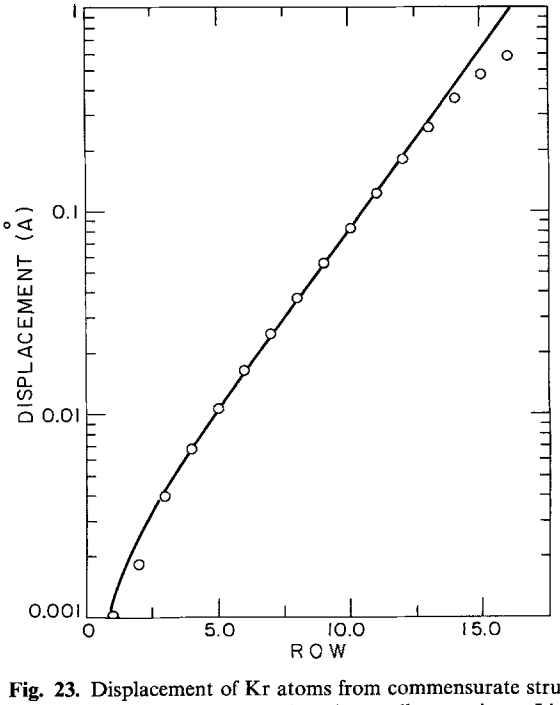

Fig. 23. Displacement of Kr atoms from commensurate structure, from domain center to domain wall crossing. Line is $D = A \sinh(ROW/2.44)$

misfit is consistent with zero-temperature predictions; while the sense of rotation is random on a macroscopic scale, single domains cover at least 1000 Å. The transition from aligned to rotated solid is distinct from the melting transition of the incommensurate phase. We proceed to consider this melting transition, which occurs just a few degrees higher in temperature.

We observed the orientational effects of the melting of the IC phase at a constant pressure of 50 Torr. Typical longitudinal and transverse scans through the Kr(100) peak are shown in Figs. 24 and 25. The longitudinal scans simply reproduce the powder substrate data with poorer counting statistics. The IC phase ($T = 104.69$ K) melts gradually into the RF phase ($T = 106.44$, $T = 107.44$), before refreezing into the C phase ($T = 108.54$). Comparing with the powder data in Figs. 5 and 6, the single crystal peaks are much sharper, both because the fluid phase remains better correlated at the lower pressure and because powder averaging makes the peaks appear broader.

The transverse scans exhibit a similar pattern. The substrate induced mosaic structure seen in the C phase ($T = 108.54$) is partially washed out even in the IC phase ($T = 104.69$) and is lost entirely as the peak

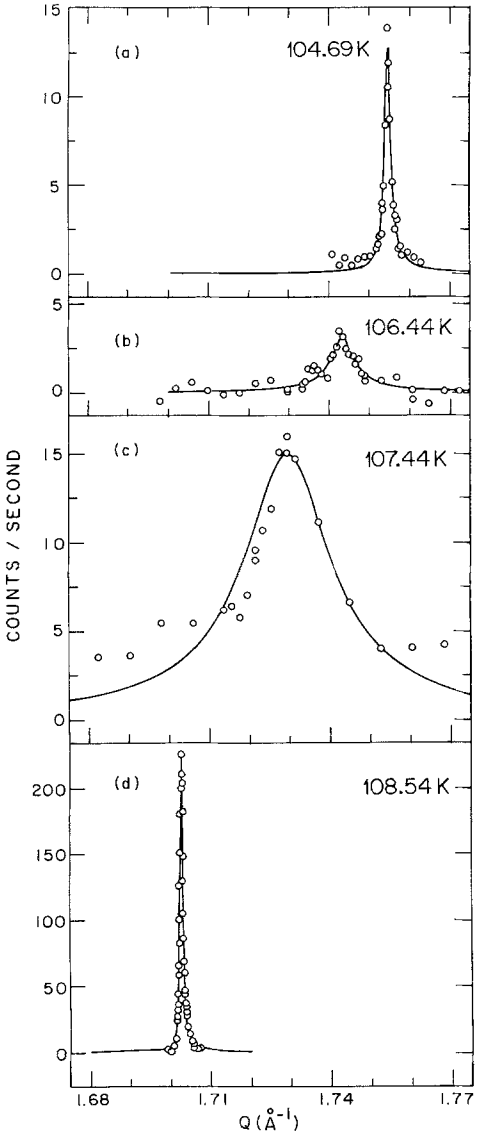

Fig. 24a–d. Longitudinal profiles of Kr(100) peak, 50 Torr: **a** 104.69 K, **b** 106.44 K, **c** 107.44 K, and **d** 108.54 K. Intensities in **a**, **b**, and **d** are to scale, intensity in **c** is increased due to instrumental considerations

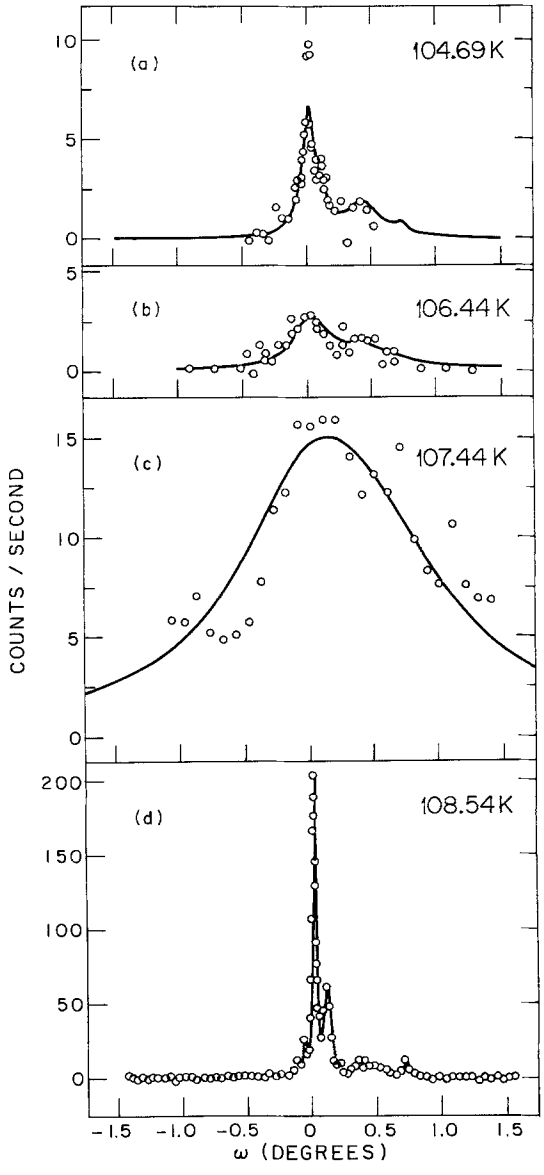

Fig. 25a–d. Transverse profiles, as Fig. 24

broadens in the RF phase ($T=106.44$, 107.44). The solid lines are the results of least squares fits to a Lorentzian lineshape, as used for the SSRL data.

The single pair of scans at $T=107.44$ is treated somewhat differently. To obtain sufficient signal from the weak scattering at this temperature, a pyrolytic Gr(0002) analyzer crystal is substituted for the Ge(111) crystal used for all other synchrotron data presented here. The incoming beam is collimated to within 0.01°, while the resolution in 2θ takes a trapezoidal profile, with a flat top 0.6° wide and a 0.18° base, defined by slits. This asymmetry between incoming and outgoing resolution produces an instrumental resolution function tilted in reciprocal space. The model lineshape is a Lorentzian convolved with this one-dimensional resolution function with a trapezoidal profile, tilted at $\theta=13.5°$ to the longitudinal direction:

$$I(q_{||}, q_{\perp})=\int R(\alpha)S(q_{||}+k_0\,\alpha\cos\theta, q_{\perp}+k_0\,\alpha\sin\theta)\mathrm{d}\alpha, \tag{36}$$

where $k_0=2\pi/\lambda=4.55\ \text{Å}^{-1}$, $\theta=13.5°$ is the Bragg angle of the monochromator, and $R(\alpha)$ is the trapezoidal resolution function. The structure factor $S(q)$ remains a convolution of Lorentzians.

Peak position is consistent with the 1/3 power law dependence of misfit on reduced temperature observed using powder substrates, as shown in Fig. 26 although clearly the data are too sparse to prove this form uniquely. The longitudinal and transverse peak widths are shown in Fig. 27. The lines in Figs. 24 and 25 are the results of fits to the lineshape given in (30), the convolution of a Lorentzian spot of width κ with a Lorentzian mosaic of width $G\Delta\theta$; the longitudinal width shown in Fig. 27 is κ, while the transverse width

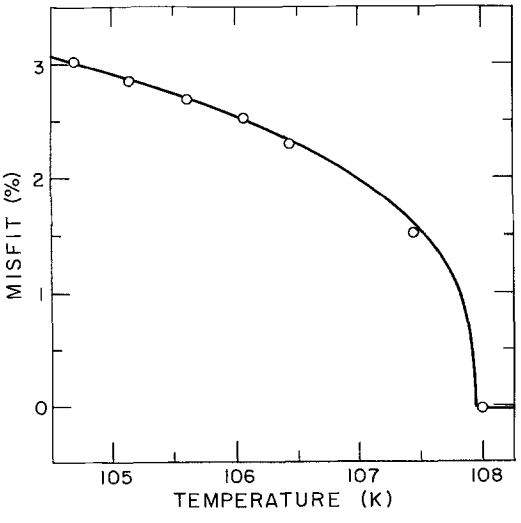

Fig. 26. 1/3 power law fit to misfit, $P=50$ Torr

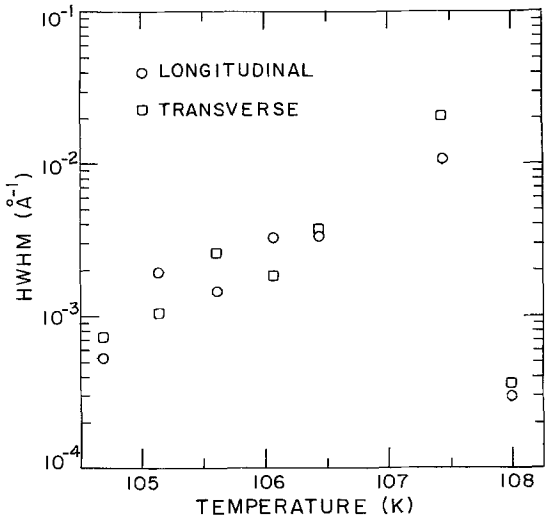

Fig. 27. Kr(100) peak width, $P=50$ Torr

is the total width $\kappa+G\Delta\theta$ including all broadening except that due to the substrate.

As discussed above the accuracy of the widths found in the incommensurate phase is limited by temperature and pressure fluctuations, which move the peak positions. The fluctuations, as measured by change in the IC phase lattice constant, correspond to temperature changes of ± 0.15 K on a time scale of about 15 min, moving the peak by amounts varying from 0.0015 to 0.005 Å^{-1}. Absolute uncertainty in either width due to all systematic errors remains about 50%. This uncertainty does not, however, affect our principal conclusion. Specifically, within these error bars, the longitudinal widths are similar to those found using powder substrates (Fig. 11b). The transverse widths do not differ significantly from the longitudinal widths: *the spots are circular, exhibiting no orientational fluctuations.*

A fluid has short range positional order. In the RF phase, approaching the RF-IC transition, the correlation length ξ diverges; on length scales less than ξ the fluid phase behaves as a solid, with well-defined crystalline axes. In an ordinary fluid, these axes will have short range orientational order, and the x-ray diffraction pattern will be a set of rings (Sect. IIA). The diffraction pattern we see in the RF phase is characteristic of a hexatic, retaining long range orientational order as the positional order diverges.

For a solid or hexatic, the response to an orientationally ordering field diverges, so only a weak perturbation by the substrate is needed to produce orientational alignment. Since the effect of the corrugation in the substrate-adsorbate potential becomes larger as the lattice misfit decreases, we must consider the possibility that the substrate provides more than

just a perturbation. Is a hexatic phase with long range orientational order characteristic of 2D melting, or is it imposed by the substrate? We will address this question by considering the orientational fluctuations we would expect in two limits, that of a hexatic phase on a smooth substrate, and that of a fluid.

Much as positional fluctuations diverge in a 2D solid, orientational fluctuations will diverge in a hexatic. Taking the limit of zero orienting field h_6 in (7), we have

$$\langle \delta\theta^2 \rangle = \frac{kT}{4\pi K_A} \ln(2L^2/\pi\sqrt{3}\xi^2), \tag{37}$$

where L is the system size, and $K_A \sim kT_c\xi^2$ is a Frank constant. The weak dependence of this result on system size introduces little uncertainty. More troublesome is the value of K_A; the theory of dislocation mediated melting gives only its scaling behavior [14], and we have no model-independent estimate.

Whatever the mechanism for the melting transition, the orientational fluctuations should have a universal amplitude. From (37), the magnitude of the fluctuations will scale as $G\Delta\theta \sim (kT/K_A)^{1/2} \sim \kappa$, giving a spot with constant aspect ratio. The strength of the Kr-Kr interaction determines the transition temperature, but drops out of the calculation of the fluctuation amplitude. Since the substrate will only reduce these fluctuations, a system with a weaker corrugation of the substrate-adsorbate potential provides a lower bound on the fluctuations expected on a smooth substrate.

Xenon on graphite provides such a system. While the actual potentials are not so different, the misfit at its melting transition is much larger, so the effect of the potential will be less. Just above the melting point of Xe the diffraction peak has transverse width 4 times its longitudinal width [16, 68], consistent with the dislocation unbinding theory of melting. Interestingly, smectic I liquid crystal films, aligned by the coupling between the director and the orientational order rather than a substrate, exhibit peaks characterized by a similar 5:1 aspect ratio in the hexatic phase [69]. Since $\langle \delta\theta^2 \rangle$ is at least 60 times less for comparable correlation lengths in the Kr system, they can hardly be melting by the same mechanism if the substrate is unimportant.

This comparison to Xe suggests that the substrate has a substantial effect on the IC-RF transition, but does not demonstrate that the substrate acts simply by supplying a field favoring alignment. As misfit decreases, the overlayer no longer responds linearly to the corrugation in substrate-adsorbate potential, but takes up the misfit in narrow domain walls. The disorder in the RF phase may be better described by defects in this lattice of domain walls than in the atomic lattice; zero-temperature energy minimization calculations show very different interactions for dislocations in the Xe atomic lattice and dislocations in the Kr domain wall lattice [55].

For this reason it is important to estimate the effect of the orienting field due to the substrate. We consider now a fluid which is rigid on length scales less than ξ but free to rotate on longer length scales, in a orienting potential per unit area $v = \frac{1}{2}h_6\theta^2$. To account for the observed $G\Delta\theta < 0.5\xi$ requires $h_6 > 1400\ \mathrm{K/\AA^2}$. The overlayer may rotate in two ways. For a weak corrugation of the Kr-Gr potential, the entire lattice will rotate by $|\theta| \approx m/\sqrt{3}$, where m is the lattice misfit. From (25), the orienting potential for small fluctuations about that minimum energy is, for a Cauchy solid,

$$h_6 = \frac{3\sqrt{3}G^2V_0}{32m^4l_0^2}. \tag{38}$$

For a stronger corrugation, most of the Kr atoms lie in commensurate domains which will not rotate; domain walls only will rotate, with orienting potential for fluctuations about the $\theta = 0$ energy minimum given by (27):

$$h_6 = \frac{3}{2}\left(\frac{1}{\sqrt{3}} - \frac{1}{2}\right) V_0 l_0 \mathrm{G}^2/\mathrm{m} \tag{39}$$

Rotation of domain walls gives a lower energy for $m < 0.76/l_0$, close to the critical misfit for rotation.

In the RF phase domain wall rotation gives the lower energy, as one would expect, since alignment with the substrate is a signature of the isolated domain wall regime. For a domain wall width $l_0 = 28$, Kr-Gr corrugation $V_0 = 10\ \mathrm{K}$, misfit $m = 2.5\%$, and Kr(100) wavevector $G = 1.746\ \mathrm{\AA}^{-1}$, the potential is, from Equation 39, $h_6 = 4000\ \mathrm{K/\AA^2}$, more than enough to account for the lack of orientational fluctuations.

While Kr/Gr exhibits a continuous IC-RF melting transition, interactions with the substrate create a strong orienting field. That the transition is continuous fulfills one major prediction of the dislocation unbinding theory of 2D melting, but we cannot test the more dramatic prediction that melting occurs in two stages, with an intermediate hexatic phase.

As shown by Fig. 27, we have examined only the IC-RF melting transition; between the point with the weakest correlations ($T = 107.44\ \mathrm{K}$) and the well-correlated C phase lies another melting transition. Since the misfit for the C-RF transition is still smaller than for the IC-RF, we expect no measurable orientational fluctuations in this region.

We are left with the phase diagram shown in Fig. 17. The results reported in this section adds the aligned-rotated transition: this dashed line assumes the transition remains at 3.5% misfit. Since we have seen

that the RF phase has a high degree of orientational order near the IC-RF transition, the aligned-rotated transition may extend into the fluid phase at higher temperatures. In the RF phase the aligned-rotated transition may be characterized by fluctuations between the two directions of rotation, terminating at an Ising type critical point.

We have reported two novel effects in this Section. We see a continuous transition from an aligned phase to one rotated away from the substrate symmetry direction, both phases being incommensurate solid monolayers. We see continuous melting of an incommensurate solid monolayer to a phase which, although it has only short range positional order, not only has long range orientational order but exhibits negligible orientational fluctuations. Both transitions may be explained by simple models describing domain walls formed in elastic media by a weak incommensurate potential, and are consistent with a domain wall width of 5 atomic rows.

We have enjoyed stimulating discussions with A.N. Berker and S.G.J. Mochrie, as well as H. Hong, to whom we are also grateful for assistance in conducting these experiments. Our last experiment made use of an excellent graphite crystal provided by H. Zabel.

This work was partially done at the Stanford Synchrotron Radiation Laboratory which is supported by the U.S. Department of Energy, Offices of Basic Energy Sciences; and the National Institutes of Health, Biotechnology Resource Program, Division of Research Resources. Further experiments were undertaken on the IBM-MIT beamlines at the National Synchrotron Light source, Brookhaven National Laboratory, which is supported by the U.S. Department of Energy, Division of Material Sciences and Division of Chemical Sciences. The MIT contributions to the operation and construction of the IBM-MIT beamlines at NSLS are supported by the National Science Foundation, Materials Research Laboratory program under grant No. DMR84-18718 and by the Joint Services Electronics Program under Contract No. DAAL03-86-K-0002. The work at MIT was supported by the U.S. Army Research Office under Contract No. DAAG29-85-K0058. One of us (E.D.S.) would like to acknowledge financial support from the National Science Foundation and an I.B.M. predoctoral fellowship.

References

1. Sinha, S.K. (ed.): Ordering in two dimensions. New York: Elsevier North Holland, 1980
2. Thomy, A., Duval, X.: J. Chim. Phys. **66**, 1966 (1969)
3. Thomy, A., Duval, X.: J. Chim. Phys. **67**, 286 (1970)
4. Thomy, A., Duval, X.: J. Chim. Phys. **67**, 1101 (1970)
5. Butler, D.M., Litzinger, J.A., Stewart, G.A.: Phys. Rev. Lett. **44**, 466 (1980)
6. Fain, S.C. Jr., Chinn, M.D., Diehl, R.D.: Phys. Rev. B **21**, 4170 (1980)
7. Stephens, P.W., Heiney, P., Birgeneau, R.J., Horn, P.M.: Phys. Rev. Lett. **43**, 47 (1979)
8. Moncton, D.E., Stephens, P.W., Birgeneau, R.J., Horn, P.M., Brown, G.S.: Phys. Rev. Lett. **46**, 1533 (1981)
9. Specht, E.D., Sutton, M., Birgeneau, R.J., Moncton, D.E., Horn, P.M.: Phys. Rev. B **30**, (1984)
10. D'Amico, K.L., Moncton, D.E., Specht, E.D., Birgeneau, R.J., Nagler, S.E., Horn, P.M.: Phys. Rev. Lett. **53**, 2250 (1984)
11. Jancovici, B.: Phys. Rev. Lett. **19**, 20 (1967); Imry, Y., Gunther, L.: Phys. Lett. **29A**, 483 (1969); Phys. Rev. **B3**, 3939 (1971)
12. Landau, L.D., Lifshitz, E.M.: Statistical physics, part 1, p. 436. Oxford: Pergamon 1980
13. Mermin, N.D.: Phys. Rev. **176**, 250 (1968)
14. Nelson, D.R., Halperin, B.I.: Phys. Rev. B **19**, 2457 (1979); Young, A.P.: Phys. Rev. B **19**, 1855 (1979)
15. Nelson, D.R.: In: Fundamental problems in statistical mechanics V, edited by Cohen, E.G.D. (ed.) New York: North Holland 1981, see also: Aeppli, G., Bruinsma, R.: Phys. Rev. Lett. **53**, 2133 (1984)
16. Nagler, S.E., Horn, P.M., Rosenbaum, T.F., Birgeneau, R.J., Sutton, M., Mochrie, S.G.J., Moncton, D.E., Clarke, R.: Phys. Rev. B **32**, 7373 (1985)
17. Birgeneau, R.J., Heiney, P.A., Pelz, J.P.: Physica (Utrecht) **109 110B**, 1785 (1982)
18. Moncton, D.E., Brown, G.S.: Nucl. Instrum. Methods **208**, 579 (1983)
19. Green, G.K.: Spectra and optics of synchrotron radiation. Report BNL 50522, April 1976
20. Busing, W.R., Levy, H.A.: Acta. Cryst. **22**, 457 (1967)
21. Putnam, F.A., Fort, T.: J. Phys. Chem. **79**, 459 (1980)
22. Larher, Y., Terlain, A.: J. Chem. Phys. **72**, 1052 (1980)
23. Suter, R.M., Colella, N.J., Gangwar, R.: Phys. Rev. B **31**, 627 (1985)
24. Miner, K. D. Jr., Chan, M.W.H., Migone, A.D.: Phys. Rev. Lett. **51**, 1465 (1983)
25. Horn, P.M., Birgeneau, R.J., Heiney, P., Hammonds, E.M.: Phys. Rev. Lett. **41**, 961 (1978)
26. Birgeneau, R.J., Brown, G.S., Horn, P.M., Moncton, D.E.: J. Phys. C **14**, L49 (1981)
27. Berker, A.N., Ostlund, S., Putnam, F.A.: Phys. Rev. B **17**, 3650 (1978)
28. Ostlund, S., Berker, A.N.: Phys. Rev. Lett. **42**, 843 (1979)
29. Chinn, M.D., Fain, S.C. Jr., Phys. Rev. Lett. **39**, 146 (1977); Fain, S.C. Jr., Chinn, M.D., Diehl, R.D.: Phys. Rev. B **21**, 466 (1980)
30. Stephens, P.W., Heiney, P.A., Birgeneau, R.J., Horn, P.M., Moncton, D.E., Brown, G.S.: Phys. Rev. B **29**, 3512 (1984)
31. Frank, F.C., van der Merwe, J.H.: Proc. R. Soc. London, Ser. A **198**, 205, 216 (1949).
32. Shiba, H.: J. Phys. Soc. Japan **46**, 1852 (1979)
33. Shiba, H.: J. Phys. Soc. Japan **48**, 211 (1980)
34. Steele, W.A.: Surf. Sci. **36**, 317 (1973)
35. Vidali, G., Cole, M.W.: Phys. Rev. B **29**, 6736 (1984)
36. Gooding, R.J., Joos, B., Bergersen, B.: Phys. Rev. B **27**, 7669 (1983)
37. Halpin-Healy, T., Kardar, M.: Phys. Rev. B **31**, 1664 (1985)
38. Bak, P., Mukamel, D., Villain, J., Wentowska, K.: Phys. Rev. B **19**, 1610 (1979)
39. Villain, J.: Two-dimensional solids and their interaction with substrates. In: *Ordering in strongly fluctuating condensed matter systems.* Riste, T. (ed.) p. 221. New York: Plenum
40. Coppersmith, S.N., Fisher, D.S., Halperin, B.I., Lee, P.A., Brinkman, W.F.: Phys. Rev. B **25**, 349 (1982)
41. Kardar, M., Berker, A.N.: Phys. Rev. Lett. **48**, 1552 (1982)
42. Huse, D.A., Fisher, M.E.: Phys. Rev. Lett. **49**, 793 (1982)
43. Abraham, F.F., Koch, S.W., Rudge, W.E.: Phys. Rev. Lett. **49**, 1830 (1982)
44. Dimon, P., Horn, P.M., Sutton, M., Birgeneau, R.J., Moncton, D.E.: Phys. Rev. B **31**, 437 (1985)
45. Clayton, G.T., Heaton, L.: Phys. Rev. **121**, 649 (1961)
46. Heiney, P.A., Stephens, P.W., Birgeneau, R.J., Horn, P.M., Moncton, D.E.: Phys. Rev. B **28**, 6416 (1983)

47. Dutta, P., Sinha, S.K.: Phys. Rev. Lett. **47**, 50 (1981)
48. McTague, J.P., Novaco, A.D.: Phys. Rev. B **19**, 5299 (1979)
49. Mochrie, S.G.J., Kortan, A.R., Birgeneau, R.J., Horn, P.M.: Z. Phys. B – Condensed Matter **62**, 79 (1985)
50. Reiter, G., Moss, S.C.: Phys. Rev. B **33**, 7209 (1986)
51. Rousseaux, F., Moret, R., Guerard, D., Lagrange, P., Lelaurain, M.: J. Phys. Lett. **45**, L111 (1984)
52. Rousseaux, F., Morett, R., Guerard, D., Lagrange, P., Lelaurain, M.: Synth. Met. **12**, 45 (1985)
53. Schobinger, M., Koch, S.W.: Z. Phys. B – Condensed Matter **53**, 233 (1983)
54. Heinekamp, S., Pelcovits, R.: Phys. Rev. B **32**, 4528 (1985)
55. Joos, B., Duesbery, M.S.: Phys. Rev. Lett. **55**, 1997 (1985)
56. Kortan, A.R., Kanel, H.V., Birgeneau, R.J., Litster, J.D.: Phys. Rev. Lett. **47**, 1206 (1981)
57. Clark, N.A.: J. Phys. **40**, C3-445 (1979)
58. Pershan, P.S., Prost, J.: J. Phys. Lett. **40**, 27 (1979)
59. Caflisch, R.G., Berker, A.N., Kardar, M.: Phys. Rev. B **31**, 4527 (1985)
60. Novaco, A.D., McTague, J.P.: Phys. Rev. Lett. **38**, 1286 (1977)
61. Villain, J.: Phys. Rev. Lett. **41**, 36 (1978)
62. Rauber, S., Klein, J.R., Cole, M.W.: Phys. Rev. B **27**, 1314 (1983)
63. Venables, J.A., Shabes-Retchkiman, P.S.: Surf. Sci. **71**, 27 (1978)
64. Shabes-Retchkiman, P.S., Venables, J.A.: Surf. Sci. **105**, 536 (1981)
65. Warren, B.E.: Phys. Rev. **59**, 693 (1941)
66. Shaw, C.G., Fain, S.C. Jr., Chinn, M.D.: Phys. Rev. Lett. **41**, 955 (1978)
67. Clarke, R., Caswell, N., Solin, S.A., Horn, P.M.: Phys. Rev. Lett. **43**, 2018 (1979)
68. Specht, E.D., Birgeneau, R.J., D'Amico, K.L., Moncton, D.E., Nagler, S.E., Horn, P.M.: J. Phys. Lett. **46**, L-561 (1985)
69. Brock, J.D., Aharony, A., Birgeneau, R.J., Evans-Lutterodt, K.W., Litster, J.D., Horn, P.M., Stephenson, G.B., Tajbakhsh, A.R.: Phys. Rev. Lett. **57**, 98 (1986)

E.D. Specht
Metals and Ceramic Division
Oak Ridge National Laboratory
Oak Ridge, Tennessee 37831
USA

A. Mak
C. Peters
R.J. Birgeneau
Department of Physics
Massachusetts Institute of Technology
Cambridge, Massachusetts 02139
USA

M. Sutton
Department of Physics
McGill University
Montreal PQ H3A 2T8
Canada

K.L. D'Amico
D.E. Moncton
Exxon Research and Engineering Co.
Annandale, New Jersey 08801
USA

S.E. Nagler
Department of Physics
University of Florida
Gainesville, Florida 32611
USA

P.M. Horn
IBM T.J. Watson Research Center
Yorktown Heights, New York 10598
USA